Degree Project in Biotechnology
Second Cycle, 30 Credits

Building Nanodisc-Based Models to Investigate CIP4 and I-BAR Function on Membranes

EBBA ROSBERG

STOCKHOLM, SWEDEN
2025

Abstract

Membrane remodeling is fundamental to cellular processes such as endocytosis, migration, and morphogenesis, and is tightly regulated by BAR domain-containing proteins. These proteins bind to membranes through their curved surfaces and often coordinate actin polymerization via interactions with signaling molecules. This thesis focused on optimizing the cloning, expression, and purification of three F-BAR domain-containing proteins—CIP4, srGAP2, and *Ce*TOCA-1—to enable functional and structural analysis using liposomes and cryo-electron microscopy (cryo-EM). Constructs were designed using various fusion tags (GST, SUMO3-eGFP, NT*) and expressed in *E. coli*. A high-salt phosphate buffer significantly improved the solubility and yield of CIP4 NT*, although residual heterogeneity remained. Cryo-EM screening revealed that CIP4 WT, but not CIP4 NT*, formed membrane tubules, suggesting that the NT*-tag may hinder membrane remodeling. The srGAP2 F-BAR domain, which functionally resembles an I-BAR domain by inducing outward curvature, showed strong liposome binding but failed to produce interpretable cryo-EM images, likely due to instability after protease cleavage. The SH3 domain of *Ce*TOCA-1 was successfully purified for future affinity-based interaction studies. Additionally, the development of circular nanodiscs is proposed as a next step for studying BAR proteins in more native-like membrane environments. These findings highlight the challenges of working with BAR domain proteins and emphasize the importance of optimizing construct design and purification strategies for high-resolution structural studies.

Keywords: BAR domain protein, membrane remodeling, protein purification, cloning, F-BAR, I-BAR, CIP4, srGAP2, *Ce*TOCA-1, fusion tags, cryo-EM, liposomes, circular nanodiscs

Sammanfattning

Membranremodellering är avgörande för cellulära processer som endocytos, cellmigration och morfogenes, och regleras av BAR-domäninnehållande proteiner. Dessa proteiner binder till membraner genom sina böjda ytor och samordnar ofta aktinpolymerisering via interaktion med signalmolekyler. Det här examensarbetet syftade till att optimera kloning, uttryck och rening av tre F-BAR-domän innehållande proteiner—CIP4, srGAP2 och *Ce*TOCA-1—för funktionell och strukturell analys med hjälp av liposomer och cryo-elektronmikroskopi (cryo-EM). Konstruktioner med olika fusionstags (GST, SUMO3-eGFP, NT*) uttrycktes i *E. coli*. En fosfatbuffert med hög salthalt förbättrade tydligt löslighet och utbyte av CIP4 NT*, även om viss heterogenitet återstod. Cryo-EM visade att CIP4 WT, men inte CIP4 NT*, bildade membrantubuli, vilket tyder på att NT*-taggen kan hämma förmågan att deformera membran. srGAP2:s F-BAR-domän, som funktionellt beter sig som en I-BAR-domän genom att inducera utåtriktad kurvatur, band starkt till liposomer men gav inga tolkbara cryo-EM-bilder, troligen på grund av instabilitet efter proteasklyvning. *Ce*TOCA-1:s SH3-domän renades framgångsrikt och är redo för framtida interaktionsstudier. Utveckling av cirkulära nanodiscar föreslås som ett nästa steg för att studera BAR-proteiner i mer naturliga membranmiljöer. Studien belyser de utmaningar som är förknippade med arbete på BAR-domänproteiner och vikten av optimerade strategier för uttryck och rening i strukturella studier.

Table of Contents

1 Introduction

Biological membranes are essential structures that define the boundaries of cells and their internal compartments. Composed primarily of self-assembling phospholipid bilayers, these membranes are dynamic, elastic, and semi-permeable, enabling them to not only compartmentalize cellular content but also to actively participate in a wide range of vital processes. These include nutrient exchange, signal transduction, immune response, and cellular events such as migration, division, and endocytosis [1, 2].

The structural integrity and adaptability of membranes are rooted in their material properties. Unlike rigid cellular components, membranes are fluid and flexible, capable of bending, stretching, and reshaping in response to environmental and cellular cues. This plasticity is crucial for maintaining homeostasis and for executing temporally and spatially regulated processes within the cell [1, 2].

The emergence of membrane-bound compartments was a pivotal step in the evolution of life. However, the very properties that made membranes advantageous—flexibility and permeability—also posed new challenges. Cells had to evolve mechanisms to tightly control membrane shape and function. One of the most fundamental aspects of this control is membrane curvature, which influences a wide array of cellular processes, from vesicle formation to protein recruitment [1].

To modulate membrane curvature, cells rely on specialized proteins, such as those in the BAR (Bin/Amphiphysin/Rvs) domain family. These proteins bind to lipid bilayers using their characteristic crescent-shaped domains, allowing them to sense, stabilize, or even induce membrane curvature. Understanding how such proteins interact with membranes—how they distinguish between different curvature states or lipid compositions—remains an active area of research, especially since their behavior can vary significantly across different experimental systems [1, 2].

Recent advances in structural biology, particularly cryo-electron microscopy (cryo-EM), in combination with synthetic membrane models such as liposomes and Nanodiscs, have enabled detailed investigations of protein–membrane interactions under near-physiological conditions. These platforms allow for precise control of membrane composition and curvature, making them ideally suited for studying how proteins like BAR domains modulate membrane shape.

1.1 BAR domain proteins

BAR domain proteins constitute a superfamily of membrane-associated scaffolding proteins that play a central role in shaping cellular membranes and coordinating cytoskeletal dynamics. They are essential for numerous biological processes, including endocytosis, cell motility, cytokinesis, organelle biogenesis, and intracellular trafficking. Their defining structural feature is the BAR domain, a crescent-shaped module composed of antiparallel coiled-coil α-helices. These domains typically form homo- or heterodimers with a conserved three-helix bundle, giving rise to a characteristic 'banana-shaped' curvature. This geometry enables BAR proteins to bind to negatively charged phospholipids and to induce or stabilize membrane curvature [1, 3-4].

The ability of BAR proteins to induce or sense membrane curvature is determined by both the intrinsic geometry of the BAR domain and the presence of accessory modules. Depending on the curvature of their dimer surface, BAR proteins can promote either inward (positive) or outward (negative) membrane deformation. Classical BAR domains typically induce narrow membrane invaginations, while F-BAR (Fes/CIP4 Homology-BAR) domains promote broader, shallower curvatures. In contrast, I-BAR (Inverse-BAR) domains stabilize protrusive, negatively curved membranes such as filopodia. Additionally, some BAR proteins, such as those containing an N-terminal amphipathic helix (N-BAR), insert this helix into the lipid bilayer to further facilitate membrane bending [1, 4].

Most BAR domain proteins are multidomain in nature, allowing them to link membrane dynamics with intracellular signaling and cytoskeletal regulation. They often include SH3 (src-homology 3) domains that mediate protein-protein interactions, as well as other regulatory motifs such as RhoGAP domains. Through these modules, BAR proteins interact with small GTPases, actin nucleators like N-WASP (Wiskott-Aldrich Syndrome Protein) and components of the Arp2/3 complex, positioning them as central integrators of membrane remodeling and actin cytoskeleton reorganization [4, 5].

Given their central role in membrane architecture and signaling, BAR proteins are implicated in various pathophysiological conditions. For example, mutations in the N-BAR protein BIN1 are associated with centronuclear myopathy and have been identified as genetic risk factors in late-onset Alzheimer's disease [6]. Overexpression or misregulation of F-BAR proteins such as CIP4 (Cdc42-interacting protein 4) has been linked to oncogenic processes, including enhanced cancer cell invasion and metastasis [7]. As such, BAR domain proteins are increasingly being explored as potential therapeutic targets in both neurological and oncological contexts.

1.1.1 F-BAR

F-BAR domains are a subclass of BAR proteins known for their ability to induce broad, shallow membrane curvature. F-BAR proteins facilitate the formation of larger, less curved structures, typically around 300 amino acids compared to classical BAR domains that are approximately 200. As dimers, F-BAR domains adopt an extended, crescent-shaped structure, approximately 20 nm in length, and exhibit significantly less curvature than classical BAR dimers. The dimers bind to negatively charged lipids on the membrane, stabilizing membrane deformation and driving invagination formation [8, 9].

F-BAR proteins function as scaffolds, coordinating the recruitment of actin-regulating complexes like N-WASP to the membrane, linking membrane curvature to actin cytoskeleton remodeling. This coupling is essential for processes such as endocytosis, where F-BAR proteins facilitate vesicle formation through the coordination of membrane invagination and actin polymerization. Additionally, F-BAR proteins are involved in cell migration and cytokinesis by regulating membrane changes during cell division and filopodia formation [10].

In human tissues, the most expressed F-BAR domain proteins are CIP4, TOCA-1, GAS7, FCHSD2, and srGAP2. Early structural studies, such as those of CIP4, revealed that the arc depth of F-BAR dimers is about three times shallower than that of classical BAR domains. However, the F-BAR subfamily exhibits significant structural diversity, with more recent studies identifying near-flat F-BAR dimers in proteins such as human GAS7 and FCHSD2 [9].

1.1.1.1 CIP4

CIP4 is a prototypical F-BAR domain protein that serves as a critical link between membrane curvature and actin polymerization. Containing an N-terminal F-BAR domain, a central HR1 domain for Cdc42 binding, and a C-terminal SH3 domain, CIP4 acts as a molecular scaffold to integrate Cdc42-mediated signaling with actin cytoskeletal dynamics. Through its SH3 domain, CIP4 recruits actin-regulatory proteins such as N-WASP, facilitating localized actin polymerization at sites of membrane deformation [11, 12].

CIP4 plays an essential role in clathrin-mediated endocytosis by recruiting actin nucleation machinery to sites of membrane invagination, promoting vesicle formation. It is also involved in the regulation of tubular structures formed from the plasma membrane and endosomes, underscoring its broader role in shaping membrane-bound compartments. By coupling membrane remodeling with cytoskeletal rearrangements, CIP4 contributes to cellular processes such as lamellipodia and filopodia formation, which are vital for cell migration and morphogenesis [11, 12].

In pathological contexts, CIP4 has been implicated in cancer progression, particularly in triple-negative breast cancer and colorectal cancer. Overexpression of CIP4 promotes the formation of invadopodia—actin-rich membrane protrusions that degrade the extracellular matrix—thereby enhancing cancer cell invasion and metastatic potential. This activity is mediated through Cdc42-dependent pathways and relies on CIP4's interaction with the actin nucleation factor N-WASP, which drives localized actin polymerization. Through its role in cytoskeletal remodeling, CIP4 represents a promising therapeutic target in invasive cancers [13, 14].

1.1.2 I-BAR

I-BAR domains represent a distinct subfamily within the BAR domain superfamily, characterized by a convex membrane-binding surface that enables them to recognize and stabilize outward, negatively curved membranes, such as those in filopodia and lamellipodia [3, 15].

Structurally, I-BAR domains form rigid, elongated dimers that align along the inner leaflet of the plasma membrane, reinforcing membrane extension. Functionally, they act as scaffolds that couple membrane deformation to actin cytoskeletal remodeling by interacting with small Rho GTPases, N-WASP and WAVE complexes. Through these interactions, I-BAR proteins coordinate localized actin polymerization at sites of membrane protrusion, enabling essential cellular processes including migration, immune cell activation, and neuronal development. Their ability to initiate and stabilize actin-driven protrusions makes them critical regulators of cell shape and motility [15, 16].

1.1.2.1 srGAP2

Slit-Robo GTPase-activating protein 2 (srGAP2) is a member of the srGAP family, which includes srGAP1 and srGAP3. All family members share a conserved domain structure comprising an N-terminal F-BAR domain, a central RhoGAP domain, and a C-terminal SH3 domain. These proteins act downstream of the Slit-Robo signaling pathway and regulate cytoskeletal dynamics by modulating small GTPases such as Cdc42 [17, 18].

Unlike classical F-BAR domains that promote membrane invagination, the F-BAR domain of srGAP2 induces outward membrane protrusions resembling filopodia. This property aligns srGAP2 with I-BAR proteins, which bind to and stabilize negatively curved membranes. srGAP2's F-BAR domain forms homodimers and can heterodimerize with srGAP1 and srGAP3, suggesting functional cooperation within the family [18, 19].

Functionally, srGAP2 is essential for neuronal morphogenesis, as it promotes filopodia formation and regulates dendritic spine development, thereby shaping synaptic structure and plasticity [18]. It also plays a role in guiding neuronal migration during cortical development. Mutations or dysregulated expression of srGAP2 have been associated with severe neurodevelopmental disorders, including early infantile epileptic encephalopathy and psychomotor impairment [20]. In addition, srGAP2 has been implicated in the regulation of tumor initiation and progression in various cancers, such as hepatocellular carcinoma [21].

1.1.3 *Caenorhabditis elegans (C. elegans)*

C. elegans is a small, transparent nematode widely used as a model organism in developmental biology, neurobiology, and genetics. It has a short life cycle, a simple and well-mapped anatomy, and can self-fertilize, making it ideal for genetic studies. With only ~1,000 somatic cells and a fully mapped nervous system of 302 neurons, it allows precise tracking of development and cell behavior. Its genome has been fully sequenced, and it is amenable to advanced genetic tools such as RNA interference and transgenesis, making it highly valuable for studying gene function and human disease mechanisms [22].

1.1.3.1 *C. elegans* TOCA 1 (*Ce*TOCA-1)

The *Ce*TOCA-1 contains conserved F-BAR and SH3 domains, and a central Cdc42-binding HR1 region, similar to its human counterpart TOCA-1. The F-BAR domain of *Ce*TOCA-1 is predicted to form a crescent-shaped dimer that binds to phospholipid membranes, inducing curvature and facilitating the formation of tubular and vesicular structures. This membrane-deforming activity mirrors that of human TOCA-1, indicating a conserved function across species [23].

The SH3 domain of *Ce*TOCA-1 interacts with the WASP homolog in *C. elegans*, known as WSP-1. This interaction is crucial for actin polymerization, as WSP-1 activates the Arp2/3 complex, leading to branched actin filament formation. Similarly, human TOCA-1's SH3 domain binds to N-WASP, facilitating actin assembly in response to signaling cues [24].

These conserved interactions highlight the essential role of TOCA-1 proteins in coordinating membrane remodeling with actin cytoskeleton dynamics—key for processes such as endocytosis and cell movement [23]. Consequently, *Ce*TOCA-1 serves as a valuable model for elucidating how BAR domain proteins regulate membrane-associated events across species.

1.2 Fusion Tags for Protein Expression and Purification

Escherichia coli (E. coli) is one of the most widely used systems for heterologous expression of recombinant proteins due to its rapid growth rate, well-characterized genetics, cost-efficiency, and capacity for high-yield production in controlled fermentations [25]. However, several limitations are associated with expressing complex or eukaryotic proteins in *E. coli*, including the absence of post-translational modifications, incorrect folding, the formation of insoluble aggregates known as inclusion bodies and sizes larger than 80-100 kDa. To address these challenges, expression vectors often incorporate fusion tags—polypeptides genetically fused to either the N- or C-terminus of the target protein—to improve yield and functionality [26].

Fusion tags serve multiple roles. Solubility tags facilitate correct folding and increase the solubility of aggregation-prone proteins, often mimicking chaperone-like functions. Common examples include the small ubiquitin-like modifier (SUMO, 11 kDa) [25, 26], the NT*-tag (~11 kDa) derived from spider silk proteins, which has shown exceptional performance in stabilizing difficult-to-express proteins [28], and green fluorescent protein (GFP, 28 kDa) [29], which aids both in solubility and in visual tracking during expression and purification. However, the effectiveness of solubility tags is protein-dependent, and empirical screening of multiple tags is often necessary [26, 27].

Affinity tags enable purification of recombinant proteins via specific and reversible binding to immobilized ligands during chromatographic separation. The hexahistidine (6×His) tag is among the most widely used, allowing purification via immobilized metal affinity chromatography (IMAC) and typically exerting minimal interference due to its small size (0.84 kDa). The glutathione S-transferase (GST) tag (26 kDa), which also enhances solubility, binds specifically to glutathione-conjugated matrices and allows purification under mild, non-denaturing conditions [26, 27].

To prevent interference with protein function, a protease recognition site is often placed between the tag and the target protein. Site-specific proteases, such as preScission and TEV protease, can then cleave the fusion tag post-purification, yielding a native or near-native protein product [26, 27].

1.3 Membrane Composition and Lipid-Protein Interactions

Cellular membranes, composed of diverse lipid species, play a crucial role in membrane function. Lipid-binding proteins are recruited to membranes through specific interactions with lipid molecules, thereby regulating key cellular processes such as signaling and trafficking. The lipid composition of the membrane—including the types of lipids present and their packing—directly affects membrane properties such as permeability, surface charge, and curvature [30, 31].

Phospholipids are the most abundant lipid species in membranes. Phosphoserine (PS) lipids, with their negatively charged headgroups, and phosphoethanolamine (PE) lipids, with neutrally charged headgroups, are key players in determining membrane structure. Phosphatidylcholine (PC) adds an additional positively charged group, choline, to the phosphate head group of phosphatidic acid. Choline is an essential nutrient required for membrane structural integrity, cell signaling, and neurotransmission [30]. PC is one of the most abundant phospholipids in cellular membranes and is found primarily in the outer leaflet of membranes [32].

Membranes can be tailored by adjusting the lipid composition, such as using dioleoyl (DO) lipids like DOPS and DOPE. These lipids are commonly used to form model membranes, such as liposomes, and can simulate the lipid composition of native cellular membranes, influencing protein-lipid interactions [30].

The interaction of peripheral proteins with membrane lipids is mediated by specialized lipid-binding domains that recognize specific lipid species. These interactions, essential for protein recruitment to membranes, regulate cellular processes such as signal transduction and membrane trafficking [30]. Liposome co-sedimentation assays are commonly used to study protein–lipid interactions, offering insights into how membrane composition influences protein binding and membrane dynamics, which is essential for understanding cellular signaling and membrane-associated diseases [30, 31].

1.4 Nanodiscs

Membrane proteins (MPs) are essential for numerous cellular processes such as signal transduction, ion transport, and energy metabolism, and they represent a significant class of drug targets. Despite their importance, MPs are challenging to study due to their hydrophobic transmembrane regions, which require a lipid environment to remain stable and soluble. Upon extraction from membranes, they often misfold or aggregate, leading to loss of function [33].

Nanodiscs have become a valuable tool to overcome these challenges. Composed of a defined lipid bilayer stabilized by amphipathic membrane scaffold proteins (MSPs), nanodiscs provide a detergent-free, near-native environment that preserves MP structure and activity. This system enables improved biochemical and structural analyses of MPs, including those that are otherwise difficult to study [33].

Recent advancements have introduced circular nanodiscs (cNDs), which provide a more homogenous sample with reduced size heterogeneity compared to traditional MSP-based nanodiscs. These are formed by covalently linking the scaffold protein's termini using the SpyCatcher-SpyTag technology, resulting in stable nanodiscs up to 50 nm in diameter. cNDs offer improved stability and reduced aggregation, making them especially well-suited for studying large membrane protein complexes and enhancing resolution in structural techniques such as cryo-EM [34, 35].

1.5 Cryo-EM

Cryo-EM is a powerful structural biology technique that enables the visualization of biological molecules at near-atomic resolution without the need for crystallization. In cryo-EM, samples are rapidly frozen in a thin layer of vitreous ice, preserving their native structure and preventing the formation of damaging ice crystals. The frozen specimens are then imaged using a transmission electron microscope at cryogenic temperatures, allowing for the capture of multiple 2D projections of the molecule from different angles [36].

One of the major strengths of cryo-EM is its ability to resolve the structures of large and dynamic biomolecular complexes that are often difficult or impossible to crystallize. Recent advances in detector technology, image processing algorithms, and electron optics have significantly increased the resolution achievable by cryo-EM, making it a key tool in drug discovery, virology, and membrane proteinresearch [1]. Cryo-EM is particularly well-suited for studying membrane proteins in lipid environments, such as nanodiscs, as it preserves the native-like conditions necessary for their stability and function [37].

Despite its strengths, cryo-EM also has limitations. Sample preparation can be technically demanding and time-consuming, and the equipment is expensive and requires specialized facilities. Furthermore, achieving high-resolution reconstructions demands large amounts of high-quality data and extensive computational resources [36].

2 Materials and Methods

2.1 Expression Constructs

Expression constructs for all forms of CIP4 and *Ce*TOCA-1 were designed using SnapGene software [38]. For srGAP2 constructs, previously available expression plasmids were utilized. The linearized vector backbones were amplified by polymerase chain reaction (PCR) [39] or site-directed mutagenesis PCR [40] where the annealing temperatures for the reactions were calculated using the Thermo Fisher Scientific™ online Tm calculator [41]. The reactions were analyzed adding 0.5 µL DpnI and using gel electrophoresis performed on 1% agarose gels containing GelRed (6X) in tris-acetate-EDTA (TAE) buffer, run at 135 V for 25 minutes. In cases where the gel displayed no bands or multiple bands, a temperature gradient PCR was employed to optimize annealing conditions. To ensure clean DNA for downstream assembly, a GeneJET PCR Purification Kit [42] was occasionally used to purify the PCR product.

Construct assembly was performed using either Rapid DNA Ligation Kit [43] or Gibson Assembly [44]. In Gibson Assembly, the vector backbones were fused with synthesized gene blocks (obtained from IDT) encoding the target proteins. Assembly reactions were prepared with an approximate vector-to-insert molar ratio of 1:3. Reactions included a self-made reaction mixture and were incubated at 50 °C for 1 hour. Control reactions omitting gene blocks were also performed to monitor background.

Ligation reactions were prepared using an approximate vector-to-insert molar ratio of 1:3. If transformations were to be performed on a later date, the ligation mixtures were stored at 0–4 °C until use.

The assembled plasmids were transformed into competent cells (*E. coli* TOP10). Competent cells were thawed on ice, and 1–10 ng of plasmid DNA was added. The mixture was incubated on ice for 30 minutes, followed by heat shock at 42 °C for 45 seconds and immediate cooling on ice for 2 minutes. Subsequently, 1 mL of Tryptic Soy Broth (TSB) medium was added, and the cultures were incubated at 37 °C on a shaking table (250 rpm) for 1 hour. Thereafter, 200 µL of the culture was plated on TSB agar plates supplemented with either ampicillin or kanamycin and incubated overnight (O/N) at 37 °C.

Three colonies from each plate were selected and inoculated into 5 mL TSB medium containing the appropriate antibiotic (ampicillin 20 µg/mL or kanamycin 50 µg/mL) at a 1:1000 inoculation ratio. Cultures were grown O/N at 37 °C with agitation.

Plasmid DNA was extracted from O/N cultures using the QIAprep Spin Miniprep Kit [45] eluated with 8 mM Tris pH8 buffer and sent for sequencing to verify the correct insertion of the target sequences. Only clones with validated sequences were used for subsequent steps.

For protein expression of *Ce*TOCA-1 SH3 domain, the validated plasmid were transformed into *E. coli* BL21 TUNER* cells. Cells were thawed on ice, and transformation was carried out by mixing 1 µL of diluted DNA (1-10 ng/µL) with 2 µL of 5X KCM solution (0.5 M KCl, 0.15 M $CaCl_2$, 0.25 M $MgCl_2$) and 7 µL Milli-Q water. After 2–5 minutes on ice, 10 µL of competent cells were added to the mixture, followed by 20 minutes of incubation on ice. Cells were then heat shocked at 42 °C for 45 seconds, after which 1 mL of TSB medium was added. Cultures were incubated at 37 °C for 1 hour before plating 200 µL onto selective agar plates containing the appropriate antibiotic. Plates were incubated O/N at 37 °C. The following day, a single colony was picked and inoculated into 5 mL of TSB medium supplemented with the corresponding antibiotic at a 1:1000 inoculation ratio, and grown O/N at 37 °C.

For all other constructs, plasmid DNA obtained from minipreps was either used directly for protein expression or stored at 4 °C until further use, without additional transformation into *E. coli* BL21 TUNER* cells.

2.2 Protein Expression

All proteins, except the *Ce*TOCA-1 SH3 Domain, were expressed using a cold induction protocol.

2.2.1 srGAP2 F-BAR Domain, CIP4 NT* and CIP4 Wild-type

The day before expression, a sterile 100 mL shake flask containing 20 mL of TSB media and 20 µL of antibiotic was inoculated with cells from a glycerol stock to generate a pre-culture. The pre-cultures were incubated O/N at 37°C on a shaking table (150 rpm). For srGAP2, kanamycin was used as the antibiotic, while ampicillin was used for the full-length CIP4 construct (CIP4 NT*) and CIP4 Wild-type (WT).

For cultivation, sterile 5 L baffled flasks containing 1 L of TSB + yeast extract (TSB+Y) media and 1 mL of antibiotic were inoculated with 10 mL of pre-culture. The cultures were incubated at 37°C on a shaking table (150 rpm). When the optical density (OD) at 600 nm reached 0.5-0.7, the cultures were shifted to 4°C for 30 minutes. After 15 minutes, the cultures were shaken to ensure uniform cooling. After 30 minutes, the cultivation was moved to 16°C on a shaking table (150 rpm). Once stabilized (approximately 20 minutes later), protein expression was induced by adding Isopropyl β-D-1-thiogalactopyranoside (IPTG).

For srGAP2 F-BAR domain, 0.5 mM IPTG was used, and for CIP4 NT* and CIP4 WT, 1 mM IPTG was used. The induced cultures were incubated O/N at 16°C on a shaking table (150 rpm). The next morning, the cell culture was harvested by centrifugation (3500 g, 4°C, 20 minutes). The supernatant was discarded, and the cell pellet was collected. If purification was to be carried out on a later day, the cell pellet was stored in a 50 mL falcon tube at -20°C.

2.2.2 *Ce*TOCA-1 SH3 Domain

The day before expression, a sterile 100 mL shake flask containing 20 mL of TSB media and 20 µL of ampicillin was inoculated with cells from an agar plate to generate a pre-culture. The pre-cultures were incubated O/N at 37°C on a shaking table (150 rpm).

For cultivation, sterile 5 L baffled flasks containing 1 L of TSB + yeast extract (TSB+Y) media and 1 mL of antibiotic were inoculated with 10 mL of pre-culture. The cultures were incubated at 37°C on a shaking table (150 rpm). When the OD reached 0.5-0.7, 1 mM IPTG was added. The cells were then expressed for 3-4 hours.

After the expression period, the cells were harvested by centrifugation (6000 g, 4°C, 15 minutes). The supernatant was discarded, and the cell pellet was collected and stored in a 50 mL falcon tube at -20°C.

2.2.3 PreScission Protease

For large-scale protein expression, *E. coli* cells were cultured in TSB+Y medium supplemented with ampicillin. Each 1 L culture was inoculated with 5 mL of a starter culture and incubated at 37 °C on a shaking table (150 rpm) until an optical density at 600 nm (OD_{600}) of 0.5 was reached. At this point, the incubator was cooled to 18 °C in preparation for induction. When the cultures reached an OD_{600} of 0.7, protein expression was induced by the addition of IPTG to a final concentration of 0.2 mM. The cultures were then incubated for an additional 24 hours at 18 °C.

Following expression, the cells were harvested by centrifugation at 4000 *g* for 15 minutes at 4 °C. The supernatant was discarded, and the cell pellet was collected and stored in a 50 mL falcon tube at -20°C.

2.3 Protein Purification and Characterization

The purification steps varied depending on the protein being processed, but the initial part of the purification process was the same for all proteins. The cell pellet was resuspended in 60 mL of respective buffer, along with a cOmplete, EDTA-free tablet (protease inhibitor cocktail, Roche). The final purification step—gel filtration—was performed on the same system, size-exclusion chromatography (SEC) using the ÄKTA go™ protein purification system, for all proteins.

2.3.1 CIP4 Constructs

The CIP4 NT* and WT proteins were processed using a lysis buffer composed of 400 mM NaCl, 50 mM phosphate buffer (pi), pH 8.0. The resuspended cells were sonicated under identical conditions: 5 seconds pulse on, 25 seconds pulse off, for a total of 4 minutes at 60% amplitude, repeated twice. Following sonication, cell debris was removed by centrifugation at 15,000 g for 1 hour at 4°C, and the resulting supernatant was collected for subsequent purification steps.

1 mL of GST beads was washed three times with water and once with lysis buffer. The washed beads were then added to the collected supernatant in a 50 mL Falcon tube and incubated for 1 hour at 4°C with gentle rotation. The resin was spun down at 500 g for 10 minutes at 4°C, and most of the supernatant was discarded. The beads were loaded onto a gravity flow column and

washed with 40-50 mL of washing buffer (400 mM NaCl, 50 mM Pi, pH 8) before the protein was eluted in 2 mL fractions using an elution buffer (400 mM NaCl, 50 mM Pi, 40 mM reduced glutathione (GSH), pH 8). The fractions concentration was measured using a Nanodrop spectrophotometer. Prescission protease (3.5 mg/mL) was then added to the entire sample at a 1:50 volume ratio to cut off the GST-tag. The mixture was incubated O/N at 4°C under gentle rotation.

If the sample concentration was too low, the sample was concentrated using a 50 kDa MWCO filter by centrifuging at 2000 g for 10 minutes at 4°C, and the supernatant was carefully removed to achieve the desired concentration. The final purification step was SEC for CIP4 NT* using a Superose 6 Increase 10/300 GL column from Cytiva. CIP4 WT was never purified using gelfiltration.

The sample was loaded onto a column equilibrated with a buffer (150 mM NaCl, 50 mM Pi, pH 8) using a 500 µL sample loop. The flow rate was set to 0.3 mL/min, and elution was collected in 0.25 mL fractions. The fractions corresponding peaks in the chromatogram were picked and further analyzed using SDS-PAGE.

2.3.2 srGAP2 F-BAR Domain

The srGAP2 F-BAR Domain were processed using a lysis buffer composed of 400 mM NaCl, 50 mM phosphate buffer, pH 8.0. The resuspended cells were sonicated with following conditions: 10-second pulse on and a 30-second pulse off for 2 minutes at 60% amplitude, repeated twice. After sonication, cell debris was removed by centrifugation at 15,000 g, 4°C for 1 hour, and the supernatant was collected for further purification.

Next, 30 mM imidazole was added to the supernatant, which was then incubated in two 50 mL Falcon tubes with 2 mL HisPur cobalt resin for 2 hours at 4°C on a rotating table. The resin was spun down at 500 g for 10 minutes at 4°C, and most of the supernatant was discarded. The resin was resuspended in the remaining supernatant and loaded onto a column. The column was washed with 40-50 mL of washing buffer (400 mM NaCl, 50 mM Pi, 30 mM imidazole, pH 8) before srGAP2 was eluted in 2 mL fractions using an elution buffer (400 mM NaCl, 50 mM Pi, 250 mM imidazole, pH 8). The fractions concentration was measured using Nanodrop.

A buffer exchange was subsequently performed, initially using PD MidiTrap™ G-25 columns [46], followed by PD-10 desalting columns packed with Sephadex G-25 resin [47]. This step was carried out to remove imidazole, which may interfere with protease activity. The fractions with the highest concentrations were pooled together in a 15 mL Falcon tube.

To test the stability of the domain, the SUMOeGFP tag was cleaved using TEV protease. A 100 µL sample was incubated with TEV protease (2.5 mg/mL) at a 1:10 volume ratio at 4°C O/N with gentle rotation. After incubation, the sample was analyzed for stability, and SDS-PAGE was performed to confirm the successful cleavage of the SUMOeGFP tag from srGAP2 F-BAR Domain.

The following day, the sample was centrifuged in 2 mL fractions at maximum speed using a tabletop centrifuge for 40 minutes at 4°C. In cases where precipitation had occurred and a pellet was observed, the supernatant was carefully transferred to a new tube. The protein concentration of the supernatant was determined using Nanodrop. Prescission protease (3.5 mg/mL) was then added to the entire sample at a 1:50 volume ratio. The mixture was incubated O/N at 4°C under gentle rotation.

If the sample concentration was too low, the sample was concentrated using a 50 kDa MWCO filter by centrifuging at 2000 g for 10 minutes at 4°C, and the supernatant was carefully removed to achieve the desired concentration. The final purification step was SEC using both a Superdex® 200 Increase 10/300 GL and a Superose 6 Increase 10/300 GL column from Cytiva. The sample was loaded onto a column equilibrated with a buffer (150 mM NaCl, 50 mM Pi, pH 8) using a 500 µL sample loop. The flow rate was set to 0.3 mL/min, and elution was collected in 0.5 mL fractions. The fractions corresponding peaks in the chromatogram were picked out. SDS-PAGE and fluorescence analysis were used to confirm which fractions contained srGAP2 F-BAR Domain and GFP. The fractions containing srGAP2 F-BAR Domain were collected.

2.3.3 *Ce*TOCA-1 SH3 Domain

The *Ce*TOCA-1 SH3 domain was processed using a lysis buffer composed of 25 mM HEPES, 300 mM KCl, pH 7.5. Sonication was performed with a 5-second pulse on and 25-second pulse off cycle for 4 minutes at 65% amplitude, repeated twice. After sonication, cell debris was removed by centrifugation at 17,000 g for 30 minutes at 4°C, and the supernatant was collected for further purification.

The supernatant was first filtered through a 1.2 μm filter followed by a 0.4 μm filter. The filtered lysate was transferred into a 50 mL Falcon tube, and 100 μL was set aside for SDS-PAGE analysis.

Meanwhile, 1 mL of GST beads was washed three times with water and once with lysis buffer. The washed beads were then added to the filtered lysate in the 50 mL Falcon tube and incubated for 1 hour at 4°C with gentle rotation. The resin was spun down at 500 g for 3 minutes at 4°C, and most of the supernatant was discarded.

The beads were then placed on ice, and the remaining supernatant was carefully poured into a new tube. The beads were loaded onto a gravity flow column, and the flow-through was collected. The column was washed with 20 column volumes (20 mL for 1 mL of beads) of lysis buffer.

Elution was performed using a buffer (25 mM HEPES, 300 mM KCl, pH 7.5, and 10 mM GSH), applying 10 column volumes and collecting 2 mL fractions. The protein concentration of each elution fraction was measured using Nanodrop.

The final purification step was SEC using a Superdex® 200 Increase 10/300 GL column from Cytiva. The lysis buffer was first filtered and degassed. The sample was loaded onto a column equilibrated with the lysis buffer using a 360 μL sample loop. The flow rate was set to 0.3 mL/min, and elution was collected in 0.5 mL fractions. The fractions corresponding peaks in the chromatogram were picked and further analyzed using SDS-PAGE.

2.4 Lipid–protein Interactions

A liposome co-sedimentation assay was performed to study lipid–protein interactions for the proteins CIP4 NT*, CIP4 WT and srGAP2 F-BAR Domain. Liposomes (1 mg/ml) were prepared with a composition of 50% DOPS and 50% DOPE. Two buffer conditions were used during the assay: a low-salt buffer containing 50 mM KCl and 20 mM HEPES at pH 7.5, and a high-salt buffer containing 40 mM HEPES, 300 mM NaCl, 20 mM imidazole, and 50 mM cholate at pH 8.0.

For each protein, three assay conditions were set up in parallel. The first served as a negative control and contained 15 μL of protein and 125 μL of low-salt buffer without liposomes. The second condition consisted of 15 μL protein, 90 μL low-salt buffer, and 30 μL of liposomes, allowing for interaction in a low-ionic-strength environment. The third condition contained 15 µL protein, 90 µL high-salt buffer, and 30 µL liposomes to test the salt sensitivity of the membrane binding.

All samples were incubated for 30 minutes at room temperature to allow for potential protein–lipid interactions. Following incubation, samples were centrifuged at 17,000 g for 40 minutes at 4°C using a tabletop centrifuge. The supernatants were carefully transferred to new 1.5 mL tubes, while the pellets were resuspended in 90 µL of the corresponding buffer (either low- or high-salt) and incubated again for 30 minutes. After this second incubation, the samples were centrifuged under the same conditions. The resulting supernatants were discarded, and the final pellets were prepared for SDS-PAGE analysis to evaluate protein binding.

To assess the proportion of protein that remained unbound, the supernatants from the first spin of the low-salt liposome condition were also analyzed by SDS-PAGE. This allowed for a direct comparison of bound versus unbound protein in response to lipid interaction under different salt conditions.

2.5 Nanodisc Reconstitution

Due to time constraints, self-constructed nanodiscs were not prepared. Nanodiscs used in this project were obtained from a previous student who had worked on a similar project. Two variants were initially evaluated: spNW50, which exhibited a low percentage of lipid-filled nanodiscs, and spNW30, which achieved approximately 57% lipid incorporation at a 1:1000 lipid-to-MSP ratio. The spNW30 construct generates circular nanodiscs (cNDs) with an approximate diameter of 32 nm. Based on these results, spNW30 was selected for subsequent experiments.

2.6 Cryo-EM

After collecting and concentrating the protein fractions, the purified protein was incubated with liposomes or nanodiscs. A 3 µL aliquot of this mixture was then applied to a cryo-EM grid and vitrified by plunge freezing. The grids were imaged at the Swedish National Cryo-EM Facility using a ThermoFisher Talos Arctica for sample optimization and data acquisition, and Titan Krios microscopes for high-resolution data collection.

3 Results

3.1 Expression Constructs

3.1.1 CIP4 Constructs

Both the CIP4 NT* and CIP4 WT constructs were cloned into the pGEX-6P-1 plasmid. The CIP4 NT* construct featured an N-terminal GST-tag and a C-terminal NT*-tag, whereas the CIP4 WT construct contained only the N-terminal GST-tag. The CIP4 NT* construct was used in five separate cloning attempts. However, both the CIP4 NT* and CIP4 WT expression constructs had already been generated in *E. coli* BL21* strains and were used directly for protein expression, purification, and characterization.

Many of these experiments were conducted in parallel, with some products from one experiment being used in subsequent ones.

3.1.1.1 Add TEV

In this experiment, we attempted to introduce a second TEV protease recognition site into the CIP4 NT* construct using the mutagenesis PCR. The goal was to enhance the cleavage efficiency of the TEV protease, as the original site appeared to be insufficiently accessible for effective enzymatic cleavage. Primers were designed to insert the second TEV site at the C-terminal end of the construct. A temperature gradient ranging from 47.8°C to 63°C was tested, with an extension time of 4 minutes during the PCR reactions. This strategy had been attempted previously without success, and similarly, our attempts did not yield successful cleavage. Given the lack of improvement and the repeated outcome, the experiment was not pursued further.

3.1.1.2 pETM11-SUMO3eGFP

We attempted to clone the CIP4 gene into the bacterial expression vector pETM11-SUMO3eGFP using Gibson assembly. This vector includes a 6×His-tag, a SUMO-tag, and a GFP-tag. The approach involved PCR amplification of the pETM11 vector backbone and the CIP4 insert, the latter including appropriate overhangs for homologous recombination. Initial efforts using mutagenesis PCR to introduce CIP4 into the vector were unsuccessful, despite repeated temperature gradient optimization (ranging from 39°C to 58°C), which can be seen in Figure 1.

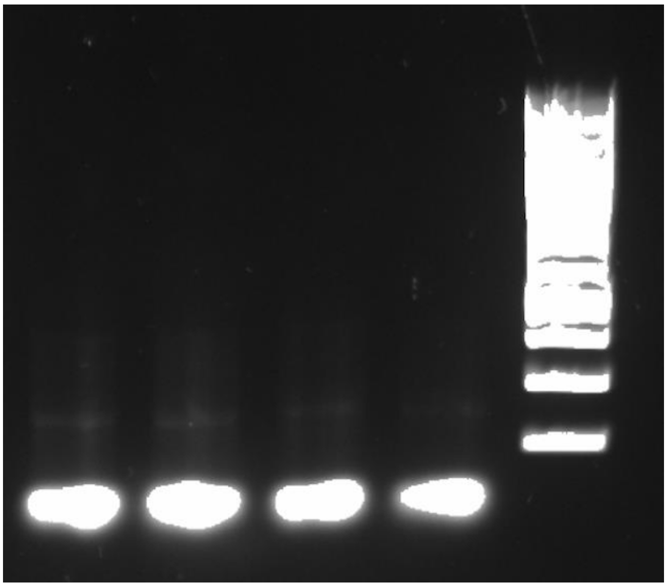

Figure 1. PCR-based mutagenesis of CIP4 in the pETM11-SUMO3eGFP vector. A temperature gradient from 54°C to 39°C was used, with an extension time of 4 minutes. Taken with BIORAD Gel Doc ™ EZ Imager.

Primers were redesigned and further attempts were made using improved constructs. A two-band pattern observed on agarose gel electrophoresis suggested partial success at 58°C, prompting restriction digestion and continued testing using Gibson assembly. This product was also used in an attempt to clone into the pAcGFP expression vector, as described in section 3.1.1.3. Despite these efforts, cloning of CIP4 into the pETM11-SUMO3eGFP vector did not result in a functional product.

3.1.1.2.1 SUMO-tag

We also attempted to add a SUMO-tag to the CIP4 NT* construct. However, the available SUMO-tag includes a GFP fusion, which adds approximately 30 kDa to the sequence. As a result, the total molecular weight of the construct approaches 100 kDa, leading to dimer formation and an overall size that is too large for our intended application.

3.1.1.3 pAcGFP

To investigate CIP4 expression in human cells and assess whether its structural features are conserved between humans and *C. elegans*, we attempted to clone the CIP4 gene into the pAcGFP expression vector. Several rounds of mutagenesis PCR were carried out in an effort to insert CIP4 into the pAcGFP vector, using different annealing temperatures and temperature gradients. Despite extensive optimization attempts, including gradient PCRs with a range of

49–72 °C, the reactions consistently failed to produce the expected amplicon using the initial primer pairs and the original vector backbone.

To address this, the pAcGFP backbone was re-amplified and restructured, yielding a successful PCR product. With a functional vector backbone available, the next step was to insert CIP4. As an alternative strategy, a purified PCR product from the CIP4 in pETM11-SUMO3eGFP construct (amplified at 58 °C) was cleaned using the QIAquick PCR Purification Kit for PCR Cleanup [48] to remove primers previously used for SUMO tagging, and then used as template DNA. $MgCl_2$ was added to the PCR mix (1 µL per 50 µL reaction) to optimize conditions, and a temperature gradient PCR with a range of 56-63 °C were executed (see Figure 2). However, despite these adjustments, the PCR failed to generate the desired construct.

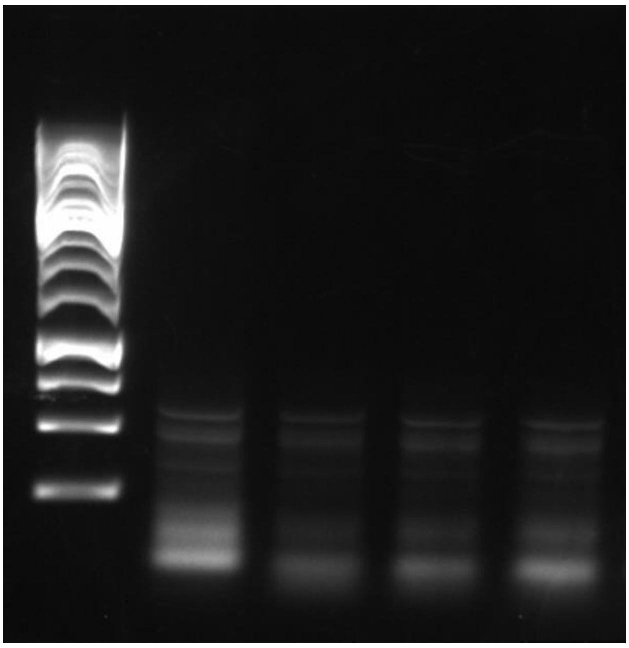

Figure 2. PCR amplification of CIP4 for insertion into the restructured pAcGFP backbone. A purified PCR product from the CIP4 in pETM11-SUMO3eGFP construct (previously amplified at 58 °C) was used as template DNA. To optimize the reaction, $MgCl_2$ was added (1 µL per 50 µL reaction), and a temperature gradient ranging from 56 °C to 63 °C was tested. Taken with BIORAD Gel Doc ™ EZ Imager.

Following repeated unsuccessful attempts, it was concluded that the original primer design might have been suboptimal. As a final step, newly designed primers were ordered and used in a renewed cloning approach with a temperature gradient of 57–49 °C. However, despite these adjustments, the cloning attempt remained unsuccessful.

3.1.1.4 pEGFP-N1

To investigate CIP4 expression in human cells and assess whether its structural features are conserved between humans and C. elegans, we attempted to clone the CIP4 gene into the pEGFP-N1 expression vector. Sequencing primers were initially selected from the manufacturer's website. The chosen reverse primer aligned with the gene of interest, although it did not span the full coding region. Since the available primers matched the pEGFP-N1 vector sequence, custom primer design was initially unnecessary.

The first plasmid construct was sent for sequencing using standard primers provided by the sequencing facility. However, the sequencing results revealed an unexpected stop codon in the CIP4 sequence, which would truncate the resulting fusion protein. To resolve this issue, new primers were designed specifically to remove the premature stop codon, and a new construct was generated and sent for sequencing. Despite these efforts, this second construct also failed to yield a functional result.

Due to time constraints, further optimization of this construct was not pursued.

3.1.2 srGAP2 F-BAR Domain

The F-BAR domain of srGAP2 was expressed using the pETM11-SUMO3eGFP construct, which had already been generated in *E. coli* BL21* strains. This expression construct encoded the F-BAR domain fused to a C-terminal SUMO-tag and GFP-tag, and included two 6×His-tags—one located upstream of the SUMO-tag and the other downstream of the GFP-tag. The construct was used for protein expression, purification, and characterization.

3.1.3 *Ce*TOCA-1 SH3 Domain

The SH3 domain of *Ce*TOCA-1 was expressed as a fusion protein with an N-terminal GST-tag on the pGEX-6P-1 plasmid. The corresponding expression construct had already been generated and was used for protein expression, purification, and characterization.

3.1.4 CeTOCA-1 F-BAR Domain

Several attempts were made to clone the F-BAR domain of *Ce*TOCA-1 into two different vectors: pGEX-6P-1 and pETM11-SUMO3eGFP. Initial cloning efforts in pGEX-6P-1 were carried out using site-directed mutagenesis PCR with primers sourced from the vector supplier. Despite multiple transformation attempts and verified plasmid yields, sequencing of several clones consistently returned incorrect or full-length *Ce*TOCA-1 sequences. Further mutagenesis PCRs were performed using gradient temperatures (e.g., 52–57 °C), which eventually yielded promising PCR products at 55 °C. However, sequencing results continued to show either the full-length gene or frameshift mutations. Due to these persistent issues, further work with the pGEX-6P-1 plasmid was discontinued, and efforts were continued solely with the pETM11-SUMO3eGFP vector.

PCR products for both the insert and pETM11-SUMO3eGFP vector were successfully amplified under optimized conditions, and Gibson assembly was used. After transformation, sequencing results again indicated problems such as the presence of a premature stop codon, which truncated the expressed protein at the GST tag. New primers were designed for both the *Ce*TOCA-1 F-BAR insert and the pETM11-SUMO3eGFP vector. A final round of mutagenesis PCR was performed under optimized conditions, using an annealing temperature of 48 °C for the vector and 60 °C for the insert. The PCR successfully produced clear bands (Figure 3) and the products were purified using the GeneJet PCR Purification Kit. These were subsequently used in a Gibson assembly reaction, followed by transformation into competent cells with kanamycin selection.

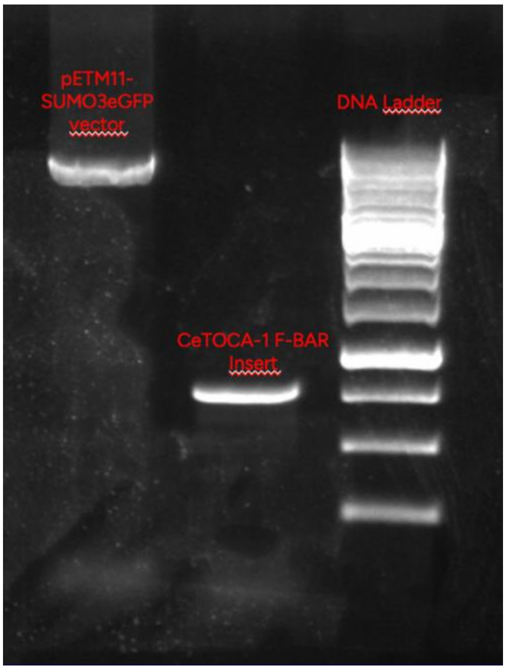

Figure 3. PCR products from the final round of mutagenesis using newly designed primers and optimized annealing temperatures (48 °C for pETM11-SUMO3eGFP and 60 °C for CeTOCA-1 F-BAR). Wall 1 corresponds to the pETM11-SUMO3eGFP vector, wall 2 to the CeTOCA-1 F-BAR insert, and wall 3 to the DNA ladder. Taken with BIORAD Gel Doc ™ EZ Imager.

3.2 Protein Expression

All protein expressions were performed according to the respective protocols outlined in Section 2.2, *Protein Expression*. The srGAP2 F-BAR Domain construct carries a kanamycin resistance marker, while the SH3 domain of *Ce*TOCA-1, CIP4 NT*, and CIP4 WT constructs are ampicillin-resistant.

The srGAP2 F-BAR Domain construct was expressed five times, CIP4 NT* and CIP4 WT construct twice. The SH3 domain was expressed once. Notably, one of the CIP4 NT* expressions were interrupted due to a power outage caused by a blown fuse or timer malfunction, which shut off the incubator during the O/N culture step.

3.3 Protein Purification and Characterization

Purification of CIP4 WT was performed, but SEC was never carried out on the purified protein. The aim of the purification was not to obtain CIP4 WT, as this had been done previously, but rather to test its stability in a 400 mM NaCl phosphate buffer. The purification of the *Ce*TOCA-1 F-BAR domain was also not completed due to issues with generating the correct expression construct. Although we managed to transform the Gibson assembly of the vector pETM11-SUMO3eGFP and the *Ce*TOCA-1 F-BAR insert, there was not enough time to proceed with further experimentation.

3.3.1 CIP4 NT*

CIP4 NT* was purified in two independent experiments using affinity chromatography (AC) followed by SEC. Between these steps, the GST-tag was successfully removed using PreScission protease to assess the stability of CIP4 retaining only the NT*-tag.

SDS-PAGE analysis of both experiments confirmed efficient tag removal. The gel from experiment one is shown in Figure 4, where a shift in band size is observed before ("bf") and after ("cut") protease treatment—from approximately 100–130 kDa to 70–100 kDa—along with the appearance of an additional band at ~25 kDa. These results are consistent with the expected molecular weights of full-length CIP4 (~80 kDa) and the cleaved GST-tag (26 kDa).

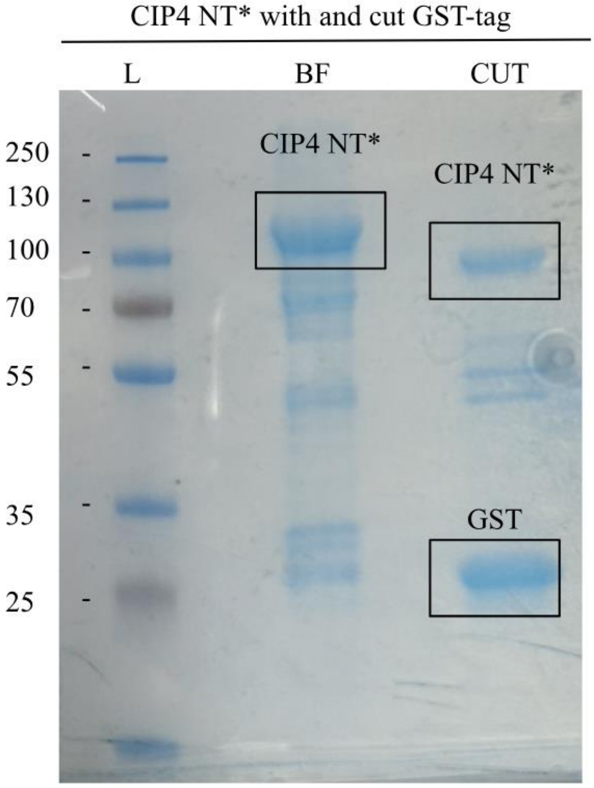

Figure 4. SDS-PAGE analysis including the ladder, the before ("bf") and after ("cut") PreScission protease treatment. A shift in band size from from approximately 100–130 kDa to 70–100 kDa is observed, along with the appearance of a smaller band at ~25 kDa.

In the first experiment, AC yielded a protein concentration of 1.544 mg/mL, as measured by Nanodrop. After O/N incubation with PreScission protease at 4 °C, SEC was performed using a Superose 6 Increase 10/300 GL column. The resulting chromatogram (Figure 5) showed a main peak at 17.81 mL, and corresponding fractions 25–28 were collected for analysis. Two additional peaks were observed: one at 13.60 mL, likely corresponding to the cleaved GST-tag, and another at 17.96 mL, the identity of which remains unclear.

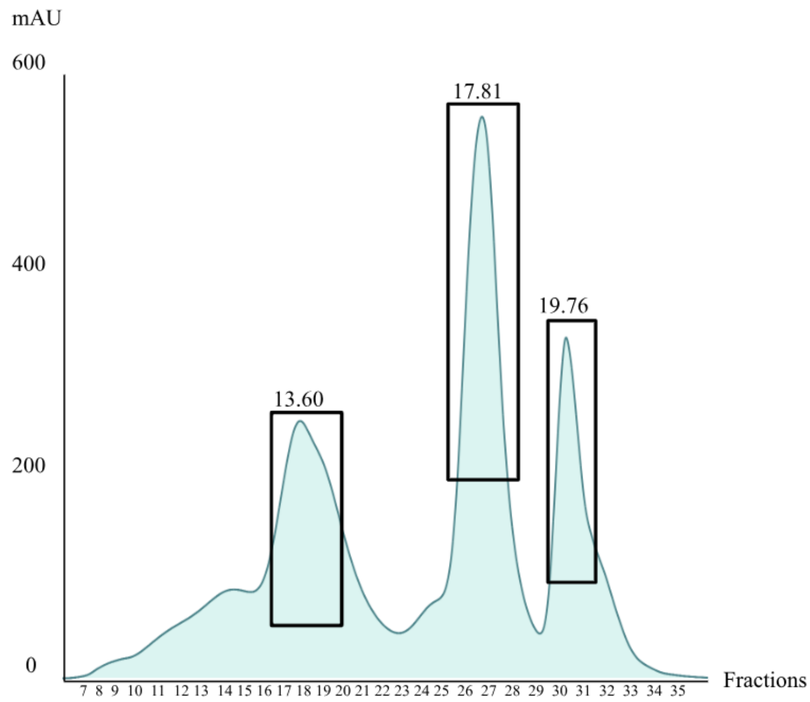

Figure 5. SEC chromatogram from the first purification experiment, performed using a Superose 6 Increase 10/300 GL column following GST-tag cleavage. The chromatogram shows a main peak at 17.81 mL, from which fractions 25–28 were collected for analysis. Additional peaks were observed at 13.60 mL—likely corresponding to the cleaved GST-tag—and at 17.96 mL, the identity of which remains uncertain.

In the second experiment, the post-AC protein concentration was 4.4 mg/mL, which decreased to 2.7 mg/mL after protease treatment and O/N incubation. SEC was conducted the following day, and fractions 38–46, corresponding to the main peak at 15.53 mL, were collected (Figure 6). As in the first run, an earlier peak at 11.17 mL likely represents the GST-tag, while a later peak at 18.62 mL remains unidentified.

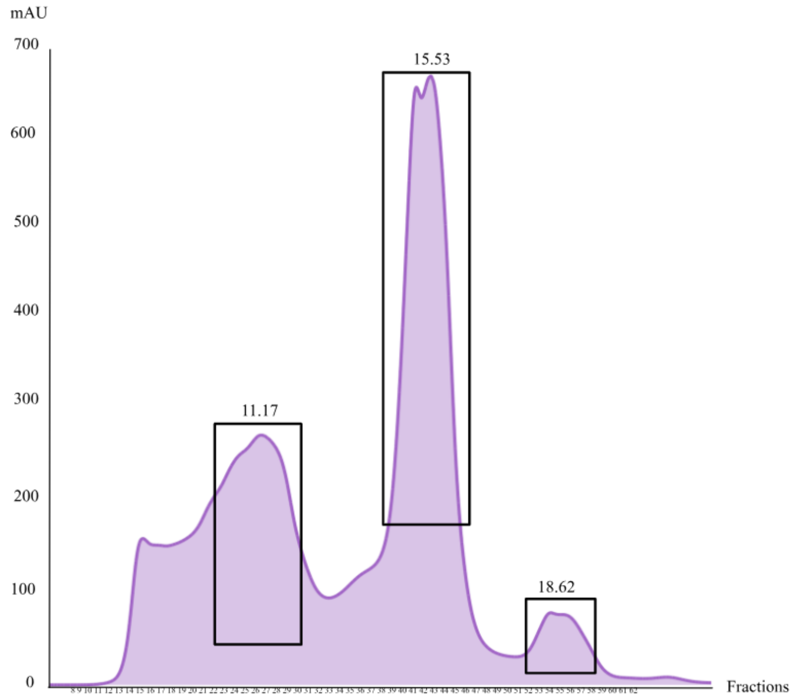

Figure 6. SEC chromatogram from the second purification experiment, conducted after O/N GST-tag cleavage. The run was performed using a Superose 6 Increase 10/300 GL column. The main peak appeared at 15.53 mL, and fractions 38–46 were collected for analysis. An earlier peak at 11.17 mL likely corresponds to the cleaved GST-tag, while a later peak at 18.62 mL remains unidentified.

3.3.2 CIP4 Wild-type

CIP4 WT was purified in a single experiment using AC. The protein concentration after AC was measured by Nanodrop and determined to be 1.21 mg/mL. Following O/N incubation with PreScission protease at 4 °C to cleave the GST-tag, the protein concentration was measured the next day and found to be 1.04 mg/mL, indicating minimal loss during the cleavage step. The sample was subsequently frozen at –20 °C for storage.

In a subsequent purification, the protein concentration reached 1.39 mg/mL after concentrating the sample threefold using a 50 kDa MWCO centrifugal filter (2000 g for 10 minutes at 4 °C). The protein precipitated subsequently and was not retained for future use.

3.3.3 srGAP2 F-BAR Domain

IMAC was performed on bacterial lysates expressing srGAP2 F-BAR domain, and the elution fractions were measured using a Nanodrop. Protein concentrations from three separate experiments are shown in Table 1.

Table 1. Protein concentrations of srGAP2 F-BAR Domain IMAC elution fractions measured using a Nanodrop spectrophotometer across three independent purification experiments.

Fraction	**Experiment 1 (mg/ml)**	**Experiment 2 (mg/ml)**	**Experiment 3 (mg/ml)**
1	0.83	0.50	0.78
2	4.77	4.18	1.75
3	1.64	3.17	0.95
4	0.43	0.52	0.19
5	0.24	0.25	0.12

The fractions with the highest protein concentrations were pooled and subjected to buffer exchange. In both experiments, buffer exchange and concentration were performed to remove imidazole—using a PD Miditrap G-25 column in the first experiment, and a PD-10 desalting column in the second. In the first experiment, after purification, the final concentration was 1.54 mg/mL.

A 100 µL aliquot of this sample was treated with TEV protease. Both the TEV-treated and untreated samples were incubated overnight at 4 °C. The following day, the TEV-treated sample showed a reduced concentration of 1.23 mg/mL. SDS-PAGE analysis showed successful cleavage, with bands corresponding to srGAP2 (~120.9 kDa) and SUMOeGFP (~39 kDa). The TEV-untreated sample remained at 1.13 mg/mL, with some precipitation observed.

Next, PreScission protease was added to the buffer-exchanged sample and incubated O/N at 4 °C. SDS-PAGE analysis confirmed successful cleavage of the SUMOeGFP-tag. The cleaved sample was then subjected to SEC using a Superdex® 200 Increase 10/300 GL column. Fractions corresponding to peaks at 7.95 mL, 11.85 mL, and 15.40 mL were collected and analyzed by SDS-PAGE (Figure 7). The corresponding chromatogram is shown in Figure 8, marked as Dataset 1. The peak at 7.95 mL corresponds to the F-BAR domain, 11.85 mL to SUMOeGFP, and 15.40 mL to srGAP2.

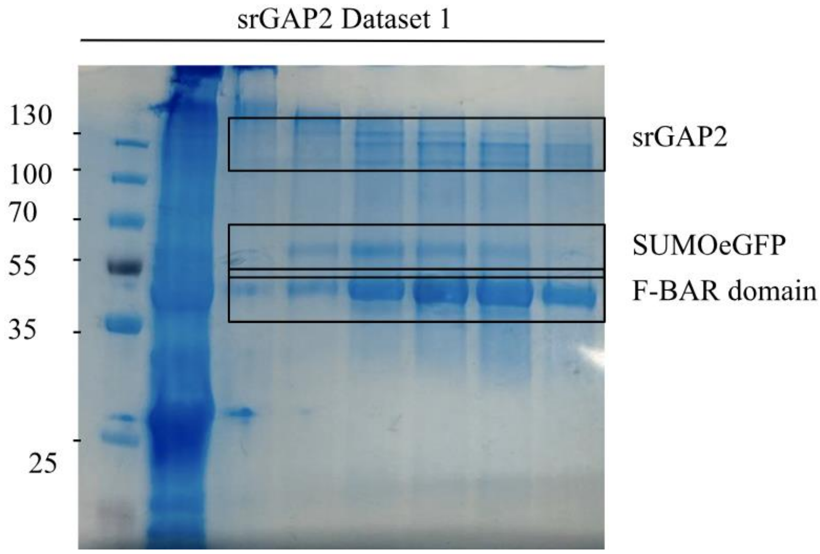

Figure 7. SDS-PAGE analysis of the SEC fractions from srGAP2 Dataset 1. The gel confirms successful cleavage of the F-BAR domain (~35.5 kDa) from srGAP2 (~120.9 kDa). A faint band corresponding to residual SUMOeGFP (~39 kDa) is still visible, indicating incomplete removal of the fusion tag.

In the second purification run, IMAC yielded a protein concentration of 9.8 mg/mL before protease treatment, which dropped significantly to 0.89 mg/mL after O/N incubation, indicating substantial protein loss due to protein precipitation. Similarly, a third purification run resulted in a lower initial concentration of 0.37 mg/mL, which further decreased to 0.22 mg/mL following protease treatment, also suggesting protein loss due to precipitation or incomplete tag cleavage.

SEC was performed for both the second (Dataset 2) and third (Dataset 3) purifications using a Superose 6 Increase 10/300 GL column. The resulting chromatograms are shown in Figure 8. The main peaks in both datasets correspond to the SUMOeGFP fusion protein (~39 kDa), while the smaller peak in Dataset 2 may correspond to uncleaved srGAP2 F-BAR domain. The expected size of the srGAP2 dimer (~120.9 kDa) suggests it would elute earlier, but this was not clearly observed, likely due to incomplete cleavage or degradation.

Despite successful purification in the first experiment, the later runs did not achieve comparable results. srGAP2 F-BAR Domain frequently precipitated, raising concerns about the stability of the purified protein. Additionally, two further srGAP2 F-BAR Domain expression cultures were prepared, but they were not processed due to a lack of active PreScission protease. Although attempts were made to express the protease, the purification could not be completed due to time limitations and lack of guidance.

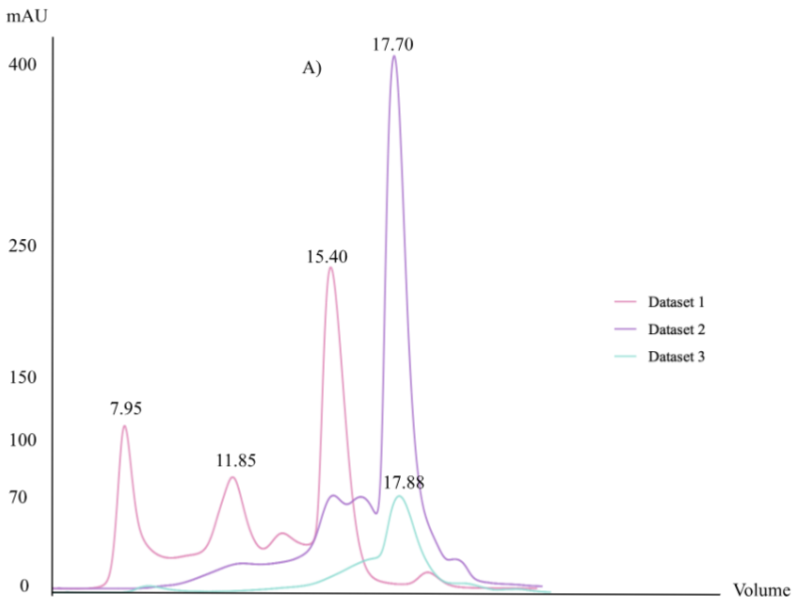

Figure 8. SEC chromatogram of three datasets following srGAP2 purification and SUMOeGFP tag cleavage. Dataset 1 (pink): Fractions from a SEC run using a Superdex® 200 Increase 10/300 GL column. Peaks at 7.95 mL, 11.85 mL, and 15.40 mL correspond to the F-BAR domain (~35.5 kDa), SUMOeGFP (~39 kDa), and srGAP2 (~120.9 kDa), respectively. SDS-PAGE confirms partial tag cleavage, with residual SUMOeGFP visible. Dataset 2 (Violet): SEC run using a Superose® 6 Increase 10/300 GL column. The dominant peak corresponds to uncut SUMOeGFP (~39 kDa), and the smaller shoulder likely reflects uncleaved srGAP2 F-BAR fusion protein. Dataset 3 (Green): Another SEC run on Superose® 6 Increase column. Only the SUMOeGFP peak is clearly visible, indicating minimal recovery of the cleaved protein.

3.3.4 *Ce*TOCA-1 SH3 Domain

The purification of the *Ce*TOCA-1 SH3 domain proceeded without complications. The protein concentrations of the elution fractions after using AC, measured by Nanodrop, which can be seen in Table 2.

Table 2. Protein concentrations of elution fractions following AC.

Fraction	**Experiment 1 (mg/ml)**
1	0.26
2	5.48
3	2.12
4	0.71

Elution fractions 2 and 3, which contained the highest protein concentrations, were pooled and concentrated by centrifugation for 1 hour, resulting in a final concentration of 15.52 mg/mL. The concentrated sample was then subjected to SEC.

Figure 9 A) shows the SEC chromatogram, and Figure 9 B) the SDS-PAGE analysis of the selected fractions (15–21), corresponding to the two elution peaks at 12.75 mL and 14.43 mL. The presence of two peaks suggests both monomeric and dimeric forms of the SH3 domain. The SH3 domain has a molecular weight of ~7.1 kDa, and as a SH3-GST fusion protein (GST: 26 kDa), the expected total molecular weight is ~33.1 kDa. SDS-PAGE analysis confirms successful purification, with a single distinct band observed at the expected size.

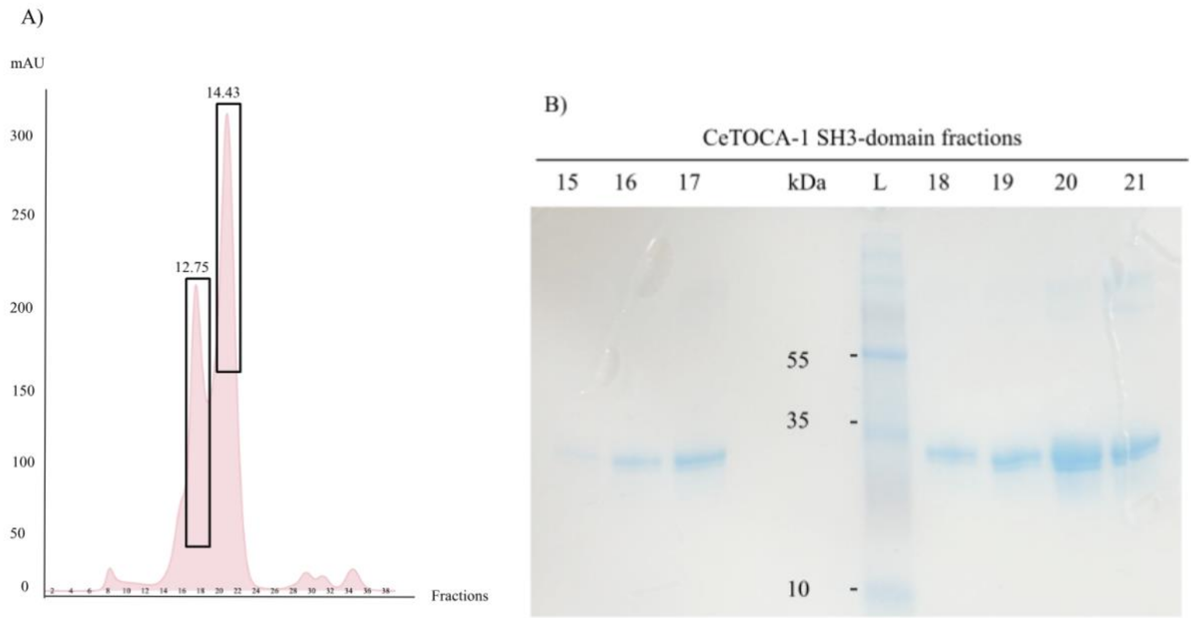

Figure 9. A) SEC chromatogram and B) corresponding SDS-PAGE analysis of the purified CeTOCA-1 SH3 domain following SEC. Selected fractions corresponding to the main elution peak (fractions 15–21) were loaded onto the gel. A molecular weight marker was loaded between fractions 17 and 18. The gel was imaged using the BIORAD Gel Doc™ EZ Imager.

3.4 Sedimentation test

A liposome co-sedimentation assay was performed to investigate the ability of CIP4 NT* and srGAP2 F-BAR Domain to bind synthetic liposomes. The assay was originally designed to include three conditions per protein: (1) protein pellet alone in low salt-buffer, (2) protein pellet with liposomes and low-salt buffer, and (3) protein pellet with liposomes under high salt conditions. However, a fourth sample was added for each protein to assess whether any protein remained in the supernatant after the first centrifugation. This allowed for additional insight into the strength of the membrane binding. The full layout which corresponds to the following setup, with each well containing the respective sample, is shown in Figure 10 and Table 3.

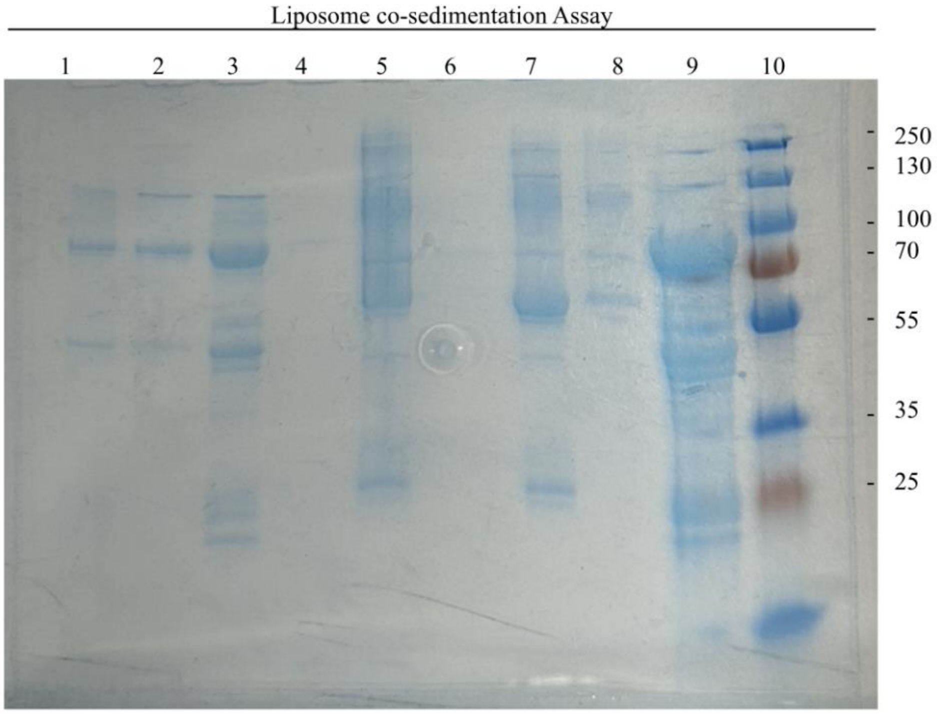

Figure 10. The SDS-PAGE analysis shows results from a co-sedimentation assay assessing liposome binding of CIP4 NT and srGAP2 F-BAR Domain. Each protein was tested under four conditions: lanes 1–4 correspond to CIP4 NT samples, and lanes 5–8 to srGAP2 F-BAR Domain samples. Lane 9 contains an unrelated sample not relevant to this assay, and lane 10 contains the molecular weight ladder.

Table 3. Sample composition of each well in the SDS-PAGE analysis from the co-sedimentation assay of CIP4 NT and the srGAP2 F-BAR domain.

Well	1	2	3	4	5	6	7	8	9	10
Sample composition	CIP4 NT* pellet + low-salt buffer	CIP4 NT* supernatant + liposomes + low-salt buffer	CIP4 NT* pellet + liposomes + low-salt buffer	CIP4 NT* pellet + high salt buffer	srGAP2 F-BAR Domain pellet + low-salt buffer	srGAP2 F-BAR Domain supernatant + liposomes + low-salt buffer	srGAP2 F-BAR Domain pellet + liposomes + low-salt buffer	srGAP2 F-BAR Domain pellet + high salt buffer	Not significant to this experiment	The ladder

The results showed that both CIP4 NT* and srGAP2 F-BAR Domain bound to liposomes, as indicated by the presence of protein in the pellet fractions (wells 3 and 7). In both cases, only weak or no bands were detected in the corresponding supernatants (wells 2 and 6), supporting the conclusion that a significant fraction of the proteins had sedimented with the liposomes.

The CIP4 NT* pellet lane showed a strong band higher on the gel, consistent with the larger size of the CIP4 (~80 kDa) relative to srGAP2 F-BAR domain (~35.5 kDa). A weaker lower band likely represents degradation, while the smallest band is assumed to be the NT*-tag.

Additionally, a separate sedimentation assay was carried out by my supervisor using CIP4 WT. This also showed successful liposome binding and was therefore included in the subsequent screening steps.

3.6 Cryo-EM

Cryo-EM samples were prepared by collecting relevant fractions after gel-filtration, concentrating them, and subsequently incubating the proteins with either liposomes (50% DOPS and 50% DOPE) or cDNs spNW30 was the thought. But when the spNW30 cNDs were initially tested for sample preparation, their concentration was found to be too low for meaningful cryo-EM screening. Consequently, liposomes were used in all main experiments.

CIP4 WT samples produced membrane tubes which can be seen in Figure 11. These tube-like structures were clearly observed in the micrographs, validating the protein's ability to induce curvature in a membrane environment. We can in Figure 11 also observe liposomes.

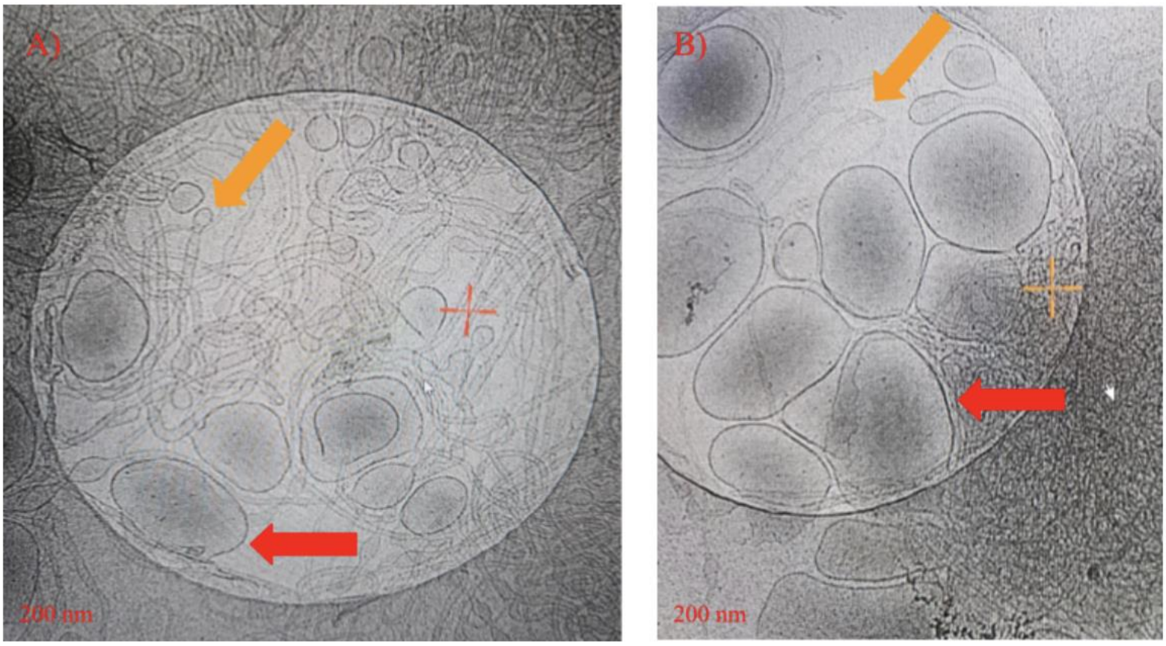

Figure 11. Both figure A) and B) show Cryo-EM micrographs of CIP4 WT incubated with liposomes composed of 50% DOPS and 50% DOPE. Tube-like membrane structures are clearly visible (pointed out with orange arrows), indicating CIP4 WT's ability to induce membrane curvature. Spherical liposomes are also present in the images, pointed out with red arrows.

Despite having a ~8–10-fold higher concentration than previously produced CIP4 NT*, this purification sample did not form tubular structures in the micrographs. Instead, only spherical liposomes were observed, which can be seen in Figure 12.

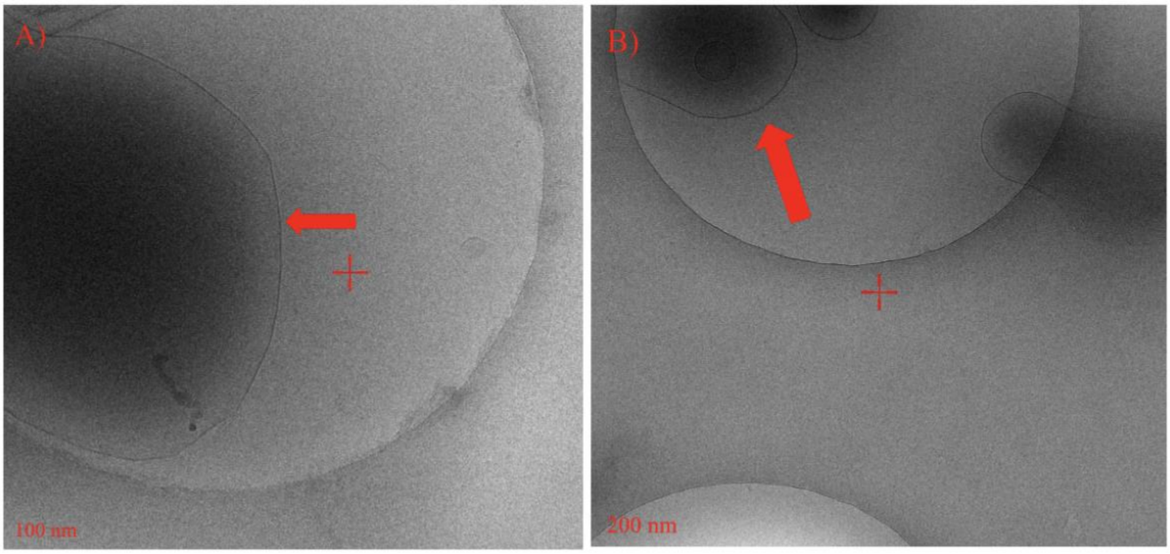

Figure 12. Both figure A) and B) show Cryo-EM micrographs of CIP4 NT incubated with liposomes composed of 50% DOPS and 50% DOPE. No membrane tubulation was observed; only spherical liposomes are visible (pointed out with a red arrow), indicating a lack of curvature-inducing activity under these conditions.*

srGAP2 F-BAR Domain samples showed liposome binding in the sedimentation assay; however, due to very low protein yield, cryo-EM screening did not produce interpretable results. As all available srGAP2 F-BAR Domain samples were consumed during initial testing, no additional cryo-EM grids could be prepared.

4 Discussion

4.1 Expression Constructs

A major bottleneck in the project was the generation of expression constructs. Issues with incorrect primers and templates led to repeated cloning attempts and significant delays, ultimately preventing the completion of key milestones such as the purification of the *Ce*TOCA-1 F-BAR domain. Although the cloning showed promising results in the end, time constraints hindered progression to protein expression and purification, as well as the full evaluation of CIP4 NT* construct.

Out of five cloning attempts for CIP4 NT*, none were successful. The efforts to clone the CIP4 gene into mammalian expression vectors (pAcGFP and pEGFP-N1) for expression in human cells were unsuccessful, despite multiple attempts using different strategies. Efforts to enhance TEV protease cleavage by introducing a second recognition site also failed. Initially, it was hypothesized that the SUMO tag alone might provide sufficient accessibility for cleavage, making the additional site redundant. However, the available construct used a SUMO3-eGFP fusion tag, which increased the total size of the protein to nearly 100 kDa. This likely contributed to dimerization and aggregation, negatively affecting expression and purification. While SUMO is generally effective in improving solubility and stability, in this context the fusion with eGFP proved counterproductive. These challenges highlight the importance of rational construct design—particularly tag size and placement—and confirm CIP4 as inherently difficult to work with.

4.2 Protein Expression

Constructs for CIP4 NT*, CIP4 WT, the F-BAR domain of srGAP2, and the SH3 domain of *Ce*TOCA-1 were already available and could be directly used for protein expression. This enabled the completion of several project milestones, including the expression of the srGAP2 F-BAR Domain. Yields were sufficient for initial cryo-EM screening, so further optimization was not performed. If needed, optimization could have been performed by adjusting temperature, IPTG concentration, or incubation time.

4.3 Protein Purification and Characterization

4.3.1 CIP4 Constructs

Efforts to purify CIP4 focused on optimizing protocols to improve solubility and stability for downstream structural studies. Given the inherent aggregation tendency of CIP4, particularly in multimeric forms, a construct combining an N-terminal GST-tag with a C-terminal NT*-tag was used to enhance solubility and facilitate purification. GST aids affinity purification and solubility, while the NT*-tag, previously shown to stabilize aggregation-prone proteins, was expected to reduce heterogeneity.

A significant advancement was made through the use of a phosphate buffer containing 400 mM NaCl, replacing the earlier HEPES-based buffers. This change resulted in an 8–10-fold increase in protein yield during purification of the CIP4 NT* construct. However, SEC revealed multiple peaks as seen in Figure 5 and 6—likely cleaved GST, CIP4 NT*, and degradation products, or even the GSH —indicating residual heterogeneity. Unfortunately, the SDS-PAGE from the SEC was lost, limiting further interpretation.

Despite improvements, the NT*-tag did not fully prevent aggregation, and the dual-tag design may interfere with structural studies by affecting the protein's native conformation. Future efforts should continue with further buffer optimization to enhance homogeneity.

CIP4 WT was also purified—not as a novel construct, but to assess its stability in the new high-salt phosphate buffer. While the initial purification showed minimal loss during GST cleavage, a second purification run resulted in complete precipitation post-cleavage, rendering the sample unusable. This indicated that the buffer did not significantly improve the stability of CIP4 WT compared to previous HEPES-based conditions used, underscoring the persistent instability of the protein.

4.3.2 srGAP2 F-BAR Domain

Purification of the F-BAR domain of srGAP2 yielded mixed results across multiple attempts. Initial expression and purification using the high-salt phosphate buffer were successful, as confirmed by SDS-PAGE in Figure 7 and SEC chromatogram in Figure 8. Distinct peaks corresponding to the srGAP2 dimer (~120.9 kDa) and the SUMO3-eGFP fusion (~39 kDa) indicated proper protease cleavage and recovery of the target protein in its dimeric form.

However, subsequent purifications were unable to replicate these initial results. Protein concentrations were markedly lower, and protease treatment frequently induced instability and precipitation. SEC chromatograms revealed incomplete cleavage and poor recovery of the srGAP2 F-BAR domain. As shown in Figure 8, the absence of well-defined BAR domain peaks in later runs strongly indicates incomplete tag removal or protein degradation. These findings suggest that tag cleavage may destabilize the protein, and factors such as bead reuse, sample freezing, and suboptimal protease activity likely contributed to degradation. Together, these issues highlight the necessity for further optimization and may reflect an inherent instability of the construct itself.

4.3.3 *Ce*TOCA-1 SH3 Domain

The rationale for maintaining the GST tag on the SH3 domain was twofold: to facilitate purification and solubility, and importantly, to use the fusion protein as an affinity reagent in future pulldown experiments. The plan is to immobilize this SH3-GST fusion on resin and pass *C. elegans* lysate through it to identify potential binding partners by analyzing proteins retained on the column. This approach aims to elucidate the interactome of *Ce*TOCA1 in *C. elegans*, providing insights into conserved functions between worms and humans.

Functionally, the presence of both monomeric and dimeric forms raises questions about the biological relevance of SH3 dimerization. In some protein families, dimerization of SH3 domains is necessary for proper function or enhanced binding affinity. However, it remains unclear whether the dimeric form observed here is physiologically relevant for *Ce*TOCA-1.

This purification served both as a practical learning exercise and as a foundational step toward functional characterization of the *Ce*TOCA-1 SH3 domain. The results establish a reliable protocol for producing the SH3 domain fusion protein in a form suitable for affinity capture experiments, which will be critical for identifying the protein's binding partners in *C. elegans* lysates and exploring evolutionary conservation of TOCA-1 function.

4.4 Cryo-EM

4.4.1 CIP4 Constructs

The liposome co-sedimentation assay confirmed strong binding of CIP4 NT* to negatively charged membranes under low-salt conditions, indicated by protein presence predominantly in the pellet fraction. This demonstrated that the NT*-tag did not impair the protein's ability to interact with membranes. Multiple bands, which can be seen in the SDS-PAGE showed in Figure 10, suggested the presence of full-length and partially degraded proteinspecies, but overall integrity was sufficient for functional interaction.

This success was supported by improved purification yields achieved by switching from HEPES-based buffers to a phosphate buffer with NaCl, which increased protein concentration 8–10-fold. The NT* tag therefore enhanced solubility and recovery, facilitating downstream assays.

However, when subjected to cryo-electron microscopy, the CIP4 NT* sample failed to induce the characteristic membrane tubulation expected of F-BAR domain proteins. Instead, only spherical liposomes were observed, indicating an absence of membrane remodeling (Figure 12). This contrasted with previous work on another BAR domain protein, FAM92A1 fused with a similar NT*-tag, which did show successful membrane tubulation [49].

The data suggest that while the NT*-tag promotes solubility and membrane binding, it may sterically hinder the conformational flexibility or oligomerization necessary for CIP4 to scaffold and deform membranes. Thus, the tag may stabilize biochemical properties but compromise functional activity related to membrane remodeling. Further experiments, particularly with tag-free CIP4, are necessary to clarify whether this inhibition is specific to the NT* fusion or a broader effect of the tagging strategy.

Supporting this, sedimentation assays performed by the supervisor on CIP4 WT confirmed membrane binding, and cryo-EM screening revealed clear tubular membrane structures (Figure 11), consistent with expected F-BAR domain activity. These tubules indicate CIP4 WT's intrinsic capacity to induce and stabilize membrane curvature. The protein concentration in these samples may have been slightly suboptimal but sufficient for observing functional membrane remodeling.

The direct comparison between CIP4 WT and CIP4 NT* highlights a critical trade-off: the NT*-tag enhances solubility and yield but appears to interfere with membrane remodeling function, whereas untagged CIP4 WT retains full activity but is more challenging to purify and stabilize.

4.4.2 srGAP2 F-BAR Domain

Similarly, liposome co-sedimentation assays confirmed that the srGAP2 F-BAR domain binds synthetic liposomes effectively, producing strong pellet fractions indicative of membrane association, seen in figure 10. Despite this, cryo-EM screening of srGAP2 samples did not yield interpretable micrographs or well-resolved BAR domain structures.

This lack of visible membrane remodeling structures likely arises from sample quality issues as previously mentioned. These factors limit the ability to capture the membrane protrusions characteristic of F-BAR domain activity and therefore I-BAR activity, despite confirmed membrane binding in sedimentation assays.

5 Future Perspectives

The overarching aim of this project was to improve the structural understanding of BAR domain proteins, with a specific focus on CIP4 and srGAP2, in the context of membrane dynamics using novel Nanodisc platforms and cryo-EM. Throughout the project, purification protocols were successfully adapted and optimized for several BAR domain-containing proteins, including CIP4 NT*, CIP4 WT, srGAP2 F-BAR, and *Ce*TOCA1 SH3 domains. Although the high-salt phosphate buffer improved CIP4 NT* yield and solubility, residual heterogeneity remained. Further optimization is needed to produce homogeneous, functional protein suitable for high-resolution structural studies.

Early setbacks and technical difficulties prevented completion of some targets, such as the purification of the *Ce*TOCA1 F-BAR domain and improved CIP4 constructs. These experiences provided valuable insights into the inherent solubility, stability, and expression challenges posed by BAR proteins—particularly CIP4, which consistently proved difficult to express and purify.

BAR proteins require customized purification strategies due to their curved, elongated shape, which alters SEC behavior and complicates size estimation. Their altered hydrodynamic properties lead to a steeper selectivity curve and lower exclusion limits, complicating direct molecular weight estimation from elution volumes. Accurate size determination would require comparison to standards of similar shape, which were not available in this project. This highlights the need for tailored analytical approaches and careful interpretation of chromatographic data when working with BAR proteins.

Unfortunately, due to time constraints, cryo-EM sample optimization as well as cryo-EM data collection and processing for CIP4 were not completed within the project timeframe. This limitation prevented the extraction of high-resolution structural insights and highlights the need for dedicated future efforts focused on sample preparation and imaging conditions.

Future work could focus on refining membrane-binding and remodeling assays by employing different MSPs and adjusting protein concentrations. For example, using PC-rich nanodiscs may better mimic native membrane environments. Imaging BAR proteins on cNDs represents a promising avenue for reconstituting their behavior in near-native lipid bilayers, facilitating more physiologically relevant structural analyses.

The challenges encountered during cloning of CIP4 into human expression vectors highlight the need for alternative approaches. Strategies such as codon optimization, gene synthesis, or exploring different mammalian expression systems could improve the success rate and expression yields of large, complex genes like CIP4 in future studies.

Compared to CIP4 constructs, srGAP2 requires substantial further optimization to improve protein stability, expression levels, and protease cleavage efficiency. These improvements are essential for high-quality cryo-EM studies and structural characterization of srGAP2's role in membrane remodeling, a process crucial for regulating neuronal morphology and synaptic development. Similarly, CIP4 participates in actin cytoskeleton remodeling and endocytic membrane curvature, linking its structural behavior to key processes in cellmigration and membrane trafficking. Understanding the architecture of both proteins at high resolution is therefore vital for elucidating their distinct yet complementary roles in shaping cellular membranes.

Despite the design of srGAP2 constructs with C-terminal SUMO and GFP fusion tags and flanking 6×His-tags aimed at promoting proper folding and purification, reproducibility across purification runs was poor. This indicates that further fine-tuning of expression conditions, protease treatments, and buffer compositions is necessary. Reliable protease activity and purification consistency will be key to overcoming these challenges in future work.

These findings highlight the delicate balance between protein stability and functional integrity, underscoring the importance of careful construct design, thorough purification optimization, and rigorous functional validation to enable successful cryo-EM studies of BAR domain proteins—efforts that will ultimately advance structural insights and deepen our understanding of membrane dynamics in health and disease.

6 Acknowledgements

I would like to express my sincere gratitude to KTH Royal Institute of Technology in Stockholm for an incredible six-year journey—beginning with the technical foundation year and continuing through my Master of Science in Biotechnology Engineering with a Medical Focus. I am deeply thankful for the outstanding education I have received and for the lifelong friendships I have formed along the way.

My heartfelt thanks go to all the teachers and lecturers whose dedication and expertise have made it possible for me to complete this master's thesis. I also wish to thank my examiner for the valuable support provided throughout this process, and my supervisor Carsten Mim for giving me the opportunity to work on this project. It has been an immensely enriching experience.

I will always be grateful to KTH. Thank you.

7 References

1. Mim C, Unger VM. Membrane curvature and its generation by BAR proteins. Trends in Biochemical Sciences. 2012 Dec;37(12):526–33.
2. Simunovic M, Voth GA, Callan-Jones A, Bassereau P. When Physics Takes Over: BAR Proteins and Membrane Curvature. Trends in Cell Biology. 2015 Dec;25(12):780–92.
3. Frost A, Unger VM, De Camilli P. The BAR domain superfamily: membrane-molding macromolecules. *Cell*. 2009;137(2):191–196.
4. Qualmann B, Koch D, Kessels MM. Let's go bananas: revisiting the endocytic BAR code. *EMBO J*. 2011;30(17):3501–3515.
5. Suetsugu S, Toyooka K, Senju Y. Subcellular membrane curvature mediated by the BAR domain superfamily proteins. *Semin Cell Dev Biol*. 2010;21(4):340–349.
6. Nicot AS, Toussaint A, Tosch V, Kretz C, Wallgren-Pettersson C, Iannaccone ST, et al. Mutations in amphiphysin 2 (BIN1) disrupt interaction with dynamin 2 and cause centronuclear myopathy. *Nat Genet*. 2007;39(9):1134–1139.
7. Cheng KW, Lahad JP, Kuo WL, Lapuk A, Yamada K, Auersperg N, et al. The RAB25 small GTPase determines aggressiveness of ovarian and breast cancers. *Nat Med*. 2004;10(11):1251–1256.
8. Itoh T, Erdmann KS, Roux A, Habermann B, Werner H, De Camilli P. Dynamin and the actin cytoskeleton cooperatively regulate plasma membrane invagination by BAR and F-BAR proteins. *Dev Cell*. 2005;9(6):791–804.
9. Snider CE, Nurul W, Hong T, Gould KL, Shiro Suetsugu. The state of F-BAR domains as membrane-bound oligomeric platforms. Trends in Cell Biology [Internet]. 2021 Apr 20 [cited 2025 May 7];31(8):644–55. Available from: https://pmc.ncbi.nlm.nih.gov/articles/PMC8286294/#ref-list1
10. Tsujita K, Suetsugu S, Sasaki N, Furutani M, Oikawa T, Takenawa T. Coordination between the actin cytoskeleton and membrane deformation by a novel membrane tubulation domain of CIP4. *Curr Biol*. 2006;16(11):1173–9.
11. Ono S, Ohashi K, Nagata M. Role of CIP4 in regulating actin dynamics and endocytic membrane trafficking. *Biochim Biophys Acta*. 2014;1843(2):217-26.
12. Frittoli E, Palamidessi A, Pece S, et al. CIP4 and its interaction with N-WASP in regulating membrane deformation during endocytosis. *Dev Cell*. 2006;10(4):555-67.

13. Hu Z, Zhu J, Ma Y, Long T, Gao L, Zhong Y, et al. CIP4 targeted to recruit GTP-Cdc42 involving in invadopodia formation via NF-κB signaling pathway promotes invasion and metastasis of CRC. Molecular Therapy - Oncolytics. 2022 Mar;24:873–86.
14. Cerqueira OLD, Truesdell P, Baldassarre T, Vilella-Arias SA, Watt K, Meens J, et al. CIP4 promotes metastasis in triple-negative breast cancer and is associated with poor patient prognosis. Oncotarget [Internet]. 2015;6(11):9397–408. Available from: https://pubmed.ncbi.nlm.nih.gov/25823823/
15. Saarikangas J, Zhao H, Lappalainen P. Regulation of the actin cytoskeleton-plasma membrane interplay by phosphoinositides. *Physiol Rev*. 2010;90(1):259–89. doi:10.1152/physrev.00036.2008.
16. Mattila PK, Lappalainen P. Filopodia: molecular architecture and cellular functions. Nat Rev Mol Cell Biol. 2008;9(6):446–454.
17. Wong K, Ren XR, Huang YZ, Xie Y, Liu G, Saito H, et al. Signal transduction in neuronal migration: roles of GTPase activating proteins and the Slit-Robo pathway. *Cell*. 2001;107(2):209–21. doi:10.1016/s0092-8674(01)00531-7.
18. Guerrier S, Coutinho-Budd J, Sassa T, Gresset A, Jordan NV, Chen K, et al. The F-BAR domain of srGAP2 induces membrane protrusions required for neuronal migration and morphogenesis. *Cell*. 2009;138(5):990–1004. doi:10.1016/j.cell.2009.06.049.
19. Coutinho-Budd J, Ghukasyan V, Zylka MJ, Polleux F. The F-BAR domains from srGAP1, srGAP2, and srGAP3 differentially regulate membrane deformation. *J Cell Sci*. 2012;125(14):3390–401. doi:10.1242/jcs.099390.
20. Saitsu H, Tohyama J, Kumada S, Egawa K, Hamada K, Okada I, et al. De novo deletions and duplications of SRGAP2 in individuals with a neurodevelopmental disorder. *Am J Hum Genet*. 2011;88(6):870–7. doi:10.1016/j.ajhg.2011.05.005.
21. Li Y, Qiao L, Bai Y, Xiao C, Wu J, Gao X, et al. Identification of SRGAP2 as a potential oncogene and a prognostic biomarker in hepatocellular carcinoma. Transl Oncol. 2021 Aug;14(8):101101. doi:10.1016/j.lfs.2021.119592.
22. National Research Council (US) Committee on Developmental Biology. *Caenorhabditis elegans: A High-Connectivity Model*. In: Development. 5th edition. Washington (DC): National Academies Press (US); 2006. Available from: https://www.ncbi.nlm.nih.gov/books/NBK20086/
23. Giuliani C, Troglio F, Bai Z, Patel FB, Zucconi A, Maria Grazia Malabarba, et al. Requirements for F-BAR Proteins TOCA-1 and TOCA-2 in Actin Dynamics and

Membrane Trafficking during Caenorhabditis elegans Oocyte Growth and Embryonic Epidermal Morphogenesis. PLOS genetics. 2009 Oct 2;5(10):e1000675–5.

24. Bu W, Lim KB, Yu YH, Chou AM, Sudhaharan T, Ahmed S. Cdc42 Interaction with N-WASP and Toca-1 Regulates Membrane Tubulation, Vesicle Formation and Vesicle Motility: Implications for Endocytosis. Rappoport JZ, editor. PLoS ONE. 2010 Aug 13;5(8):e12153.
25. Rosano GL, Ceccarelli EA. Recombinant protein expression in *Escherichia coli*: advances and challenges. *Front Microbiol*. 2014;5:172.
26. Costa S, Almeida A, Castro A, Domingues L. Fusion tags for protein solubility, purification and immunogenicity in Escherichia coli: the novel Fh8 system. Frontiers in Microbiology. 2014;5(63).
27. Zhao X, Li G, Liang S. Several Affinity Tags Commonly Used in Chromatographic Purification. Journal of Analytical Methods in Chemistry [Internet]. 2013;2013:1–8. Available from: https://www.hindawi.com/journals/jamc/2013/581093/
28. Sarr M, Kronqvist N, Chen G, Rihards Aleksis, Pasi Purhonen, Hebert H, et al. A spidroin-derived solubility tag enables controlled aggregation of a designed amyloid protein. The FEBS Journal. 2018 Apr 14;285(10):1873–85.
29. Green Fluorescent Protein (GFP) Control Protein [Internet]. Rockland.com. 2016 [cited 2025 May 6]. Available from: https://www.rockland.com/categories/proteins-and-peptides/green-fluorescent-protein-gfp-control-protein-000-001-215/?srsltid=AfmBOopTYzGRbenGgE9FrR1h93xJdKo-oFg70Wa5kNU-qmQ9lbg-O3jj
30. Bigay J., Antonny B. Curvature, lipid packing, and electrostatics of membrane organelles: defining cellular territories in determining specificity. *Dev Cell*. 2012;23(5):886-895. doi:10.1016/j.devcel.2012.10.009.
31. Senju Y., Lappalainen P., Zhao H. Liposome co-sedimentation and co-flotation assays to study lipid–protein interactions. *Methods in Cell Biology*. 2013;121:151-163. doi:10.1016/B978-0-12-420124-9.00008-X.
32. Waite KA, Vance DE. Dimethylethanolamine does not prevent liver failure in phosphatidylethanolamine N-methyltransferase-deficient mice fed a choline-deficient diet. Biochimica et Biophysica Acta (BBA) - Molecular and Cell Biology of Lipids. 2004 Mar;1636(2-3):175–82.

33. Padmanabha Das KM, Shih WM, Wagner G, Nasr ML. Large Nanodiscs: A Potential Game Changer in Structural Biology of Membrane Protein Complexes and Virus Entry. Frontiers in Bioengineering and Biotechnology. 2020 Jun 12;8.
34. Nasr ML, Baptista D, Strauss M, Sun ZYJ, Grigoriu S, Huser S, et al. Covalently circularized nanodiscs for studying membrane proteins and viral entry. Nature Methods [Internet]. 2017 Jan 1 [cited 2023 May 24];14(1):49–52. Available from: https://www.nature.com/articles/nmeth.4079
35. Zhang S, Ren Q, Novick SJ, Strutzenberg TS, Griffin PR, Bao H. One-step construction of circularized nanodiscs using SpyCatcher-SpyTag. Nat Commun. 2021;12(1):5451. doi:10.1038/s41467-021-25737-7
36. Kremer JR, Baumeister W. Cryo-Electron Microscopy: The Principle, Strengths, Limitations, and Applications. *Technology Networks*. 2020. Available from: https://www.technologynetworks.com/analysis/articles/cryo-electron-microscopy-principle-strengths-limitations-and-applications-377080
37. Šolinc G, Srnko M, Merzel F, Crnković A, Kozorog M, Podobnik M, et al. Cryo-EM structures of a protein pore reveal a cluster of cholesterol molecules and diverse roles of membrane lipids. Nature Communications [Internet]. 2025 Mar 26 [cited 2025 Apr 13];16(1). Available from: https://pubmed.ncbi.nlm.nih.gov/40140423/
38. SnapGene | Software for everyday molecular biology [Internet]. SnapGene. Available from: https://www.snapgene.com
39. Thermo Scientific Phusion High-Fidelity PCR Kit #_ Lot _ Expiry Date _ Store at -20 °C [Internet]. 2016. Available from: https://tools.thermofisher.com/content/sfs/manuals/MAN0013363_Phusion_HiFi_PCR_Kit_UG.pdf
40. Site-Directed Mutagenesis Kit Catalog Number F541 [Internet]. Available from: https://assets.thermofisher.com/TFS-Assets/LSG/manuals/MAN0013377_Phusion_SiteDirected_Mutagenesis_UG.pdf
41. Thermo Fisher Scientific. Tm calculator [Internet]. Waltham (MA): Thermo Fisher Scientific; [cited 2025 May 2]. Available from: https://www.thermofisher.com/se/en/home/brands/thermo-scientific/molecular-biology/molecular-biology-learning-center/molecular-biology-resource-library/thermo-scientific-web-tools/tm-calculator.html
42. Thermo Fisher Scientific. GeneJET PCR Purification Kit user manual [Internet]. Waltham (MA): Thermo Fisher Scientific; [cited 2025 May 2]. Available from:

https://static.igem.org/mediawiki/2017/8/81/T--Chalmers-Gothenburg--Thermo_Scientific_GeneJET_PCR_Purification_Kit.pdf
43. Thermo Fisher Scientific. Rapid DNA Ligation Kit User Guide [Internet]. 2012 [cited 2025 May 7]. Available from: https://assets.thermofisher.com/TFS-Assets/LSG/manuals/MAN0012709_Rapid_DNA_Ligation_UG.pdf
44. New England Biolabs. Gibson Assembly protocol (E5510) [Internet]. Ipswich (MA): New England Biolabs; [cited 2025 May 2]. Available from: https://www.neb.com/en/protocols/2012/12/11/gibson-assembly-protocol-e5510
45. QIAGEN. QIAprep Spin Miniprep Kit Handbook [Internet]. Hilden (Germany): QIAGEN; [cited 2025 May 2]. Available from: https://www.qiagen.com/se/resources/resourcedetail?id=c1276626-d0b2-4e95-b2c3-dc81803a198c&lang=en
46. Cytiva. PD Miditrap G-25 [Internet]. Marlborough (MA): Cytiva; [cited 2025 May 14]. Available from: https://www.cytivalifesciences.com/en/us/shop/chromatography/prepacked-columns/desalting-and-buffer-exchange/pd-miditrap-g-25-p-06181
47. Cytiva. Sephadex G-25 in PD-10 Desalting Columns [Internet]. Marlborough (MA): Cytiva; [cited 2025 May 2]. Available from: https://www.cytivalifesciences.com/en/us/shop/chromatography/prepacked-columns/desalting-and-buffer-exchange/sephadex-g-25-in-pd-10-desalting-columns-p-05778
48. QIAquick PCR Purification Kit [Internet]. www.qiagen.com. Available from: https://www.qiagen.com/zh-us/products/discovery-and-translational-research/dna-rna-purification/dna-purification/dna-clean-up/qiaquick-pcr-purification-kit
49. Wang Z, Mim C. Optimizing purification of the peripheral membrane protein FAM92A1 fused to a modified spidroin tag. Protein Expr Purif. 2022;189:105992. doi:10.1016/j.pep.2021.105992.